TITLE

Matrix Inversion and Subset Selection (MISS): A novel pipeline for quantitative mapping of diverse cell types across the murine brain

Mezias, Christopher[1*]; Torok, Justin[1*]; Maia, Pedro D.[2]; Raj, Ashish[2]
[1]Weill Cornell Medicine – New York, NY, United States
[2]Department of Radiology, University of California, San Francisco – San Francisco, CA, United States
*These authors are co-first authors who contributed equally to this work.

Correspondence should be directed to Ashish Raj (ashish.raj@ucsf.edu)

ABSTRACT

The advent of increasingly sophisticated imaging platforms has allowed for the visualization of the murine nervous system at single-cell resolution. However, current cell counting methods compromise on either the ability to map a large number of different cell types, or spatial coverage, and therefore whole-brain quantification of finely resolved neural cell subtypes remains elusive. Here we present a comprehensive and novel computational pipeline called Matrix Inversion and Subset Selection (MISS) that aims to fill this gap in knowledge and has the ability to infer counts of diverse collections of neural cell types at sub-millimeter resolution using a combination of single-cell RNAseq and *in situ* hybridization datasets. We rigorously demonstrate the accuracy of MISS against literature expectations, and in so doing, provide the first verified maps for twenty-five distinct neuronal and non-neuronal cell types across the whole mouse brain. The resulting comprehensive cell type maps are uniquely suited to address important open questions in neuroscience. As a demonstration, we utilize our inferred maps to quantitatively establish that adult cell type distributions reflect the ontological splits between brain regions during neural development, indicating that the developmental history of brain regions informs their final cell-type composition. Although this link has been frequently surmised by neuroscientists, its quantitative verification across the entire brain has not previously been demonstrated. Together, our results suggest that the MISS pipeline can be used to generate accurate spatial quantification of diverse cell types without the direct imaging of known type-specific markers, as has been done previously. The entire MISS pipeline and outputs will be made open source in order to catalyze future neuroscientific advances across disciplines.

INTRODUCTION

Characterizing whole-brain distributions of different neural cell types, especially different subtypes of GABAergic (inhibitory), glutamatergic (excitatory) cells, is a topic of keen interest in modern neuroanatomy with many applications to both basic and clinical neuroscience research. Advances in molecular methods for quantifying gene expression and data analytic cell clustering techniques based on morphologic or genetic profiles[1–8] are beginning to enable the mapping of meso-and-microscale neuronal and non-neuronal cell type architecture at a whole-brain scale. Pioneering work mapping single-cell RNA sequencing (scRNAseq) data from aquatic flatworms and zebrafish onto *in situ* hybridization (ISH)

expression provides a plausible route to mammalian cell-type mapping in the nervous system[9,10]. Whole-brain cell type mapping has historically focused on neuromodulatory systems, largely because the identification of catecholamine-producing subpopulations using molecular markers[11–14] is rather straightforward. More recently, serial 2-photon tomography (STPT) imaging cells expressing individual cell type markers genetically tagged to green fluorescent protein (GFP) successfully mapped three important subpopulations of inhibitory GABAergic interneurons, Pv+, Sst+, and Vip+ cells[1], and cholinergic neurons[15]. Although this technique is accurate and covers the entire brain, it is labor and computationally intensive, while limited to only neuronal subtypes with known, distinct molecular markers. Therefore, mapping large and diverse sets of cell subpopulations across the entire murine brain remains challenging[16].

Whole-brain mapping of broad classes of neuronal and glial subpopulations at single-cell resolution was demonstrated using purely computational methods[5], with the limitation that the mapped cell types required unique identification via a single molecular marker. Other groups have successfully mapped more specific cell types in small fractions of the total mouse brain volume, including the visual cortex[4], somatosensorty cortex[7], and hypothalamus[8] at single-cell resolution. Current literature therefore points to a tradeoff between number of unique cell types simultaneously mapped, referred to herein as cell type "specificity," and breadth of spatial coverage (See **Table 1**). Consequently, available cell type maps are not fully suited to answer macroscale questions about nervous system organization and functionality.

The present research eliminates this tradeoff, yielding quantitative maps of absolute numbers of cells across the whole brain without sacrificing either cell type specificity or spatial coverage. As illustrated in **Table 1**, our approach accurately resolves 25 neuronal and glial cell types from an scRNAseq dataset with whole brain coverage at sub-millimeter spatial resolution. Three key methodological innovations make this possible. **First**, we employ a matrix of known single-cell gene expression obtained from scRNAseq data, thereby moving away from single cell markers[1,5,11–14] and instead incorporating all available and relevant information across genes and cell types. We perform non-negative constrained inversion of this matrix, similar to Grange *et al*[17], who first applied this approach using microarray data. **Second**, we report that it is necessary to remove a large number of genes prior to matrix inversion. These genes may negatively impact cell count estimation in two principal ways: 1) nonspecific genes add noise; and 2) genes that are expressed at high levels, but not in any of the 25 types tested here, would amplify prediction error; i.e. the "missing cell types" problem[17]. Therefore, we implemented a series of principled subset selection methods using various information-theoretic criteria to rank and select genes. In particular, we propose a novel approach augmenting the minimum redundancy criterion[18] with a projection error term, which was found to outperform other selection methods. **Third**, we optimized our pipeline using several objective metrics and empirical datasets from prior publications. This methodological pipeline, which we call **Matrix Inversion with Subset Selection (MISS)**, yields fully quantitative maps of highly specific cell types in each voxel in the brain, an outcome which was not previously possible[17].

We demonstrate that MISS, after optimizing its internal parameters, produces excellent agreement both quantitatively and qualitatively to type-specific estimates from several literature studies across multiple distinct cell types[1,19]. Using layer-specific glutamatergic neurons[6], we were also able to recreate canonical neocortical laminar ordering with high fidelity. All 25 type-specific maps are available for download along with the MISS pipeline, which is designed to grow over time and to easily accommodate additional scRNAseq data for further cell type coverage. These maps constitute, to our knowledge, the most comprehensive whole brain cell type quantification currently available.

Finally, we demonstrate MISS' scientific utility by applying our inferred maps to the following outstanding question: How well do adult cell type distributions continue to reflect known divisions from neural developmental ontology? We show here, for the first time, that inter-regional cell type similarity can be used to recreate the major divisions of the brain during neural development. Together, our results both validate the proposed technique as well as demonstrate its utility in several ways.

Study	Description of Methodology Used	Neural Cell Types Mapped	Spatial Coverage	Cell Counts
Present study	**MISS using the ABI ISH gene expression atlas[20] and scRNAseq-based type-specific transcriptomic profiles[6,21]**	**25[a]**	**Whole brain**	**Yes**
Wang *et al*, 2018[4]	1020 unique genes imaged at single-cell resolution in intact mouse brain tissue using STARmap	16[b]	Primary visual cortex	Yes
Moffitt *et al*, 2018[8]	155 unique genes imaged at the single-cell level using MERFISH, with type-specific markers identified by scRNAseq	>70[c]	Hypothalamic preoptic region	Yes
Codeluppi *et al*, 2018[7]	33 type-specific marker genes imaged at the single-cell level using osmFISH	31[d]	Somatosensory cortex	Yes
Murakami *et al*, 2018[3]	Single nuclei of cells imaged and detected using light-sheet fluorescence microscopy within CUBIC-X-cleared whole mouse brains	1	Whole brain	Yes
Erö *et al*, 2018[5]	ABI ISH gene expression atlas and Nissl stain atlas[cite] coregistered computationally and cells of specific types identified and counted using single molecular markers	8[e]	Whole brain	Yes
Kim *et al*, 2017[1]	Transgenic mouse lines expressing FP-tagged interneuron markers imaged using serial two-photon tomography (qBrain)	3[f]	Whole brain	Yes
Grange *et al*, 2014[17]	Matrix inversion using the ABI ISH gene expression atlas[cite] and microarray-based type-specific transcriptomic profiles[cite]	64[g]	Whole brain	No
Herculano-Houzel *et al*, 2013[22]	Brain tissue from different regions separated into neurons and non-neuronal cells using an isotopic fractionator and quantified	2[h]	18 regions, primarily neocortical	Yes

a See text and S. Table 1
b Various glutamatergic and GABAergic neurons; oligo.; astro.; micro.; endothelial cells; other non-neuronal cells
c Various glutamatergic and GABAergic neurons; oligo.; astro.; micro.; endothelial cells; other non-neuronal cells
d Various glutamatergic and GABAergic neurons; oligo.; astro.; micro.; endothelial cells; other non-neuronal cells
e Glutamatergic, GABAergic, serotonergic, dopaminergic, and cholinergic neurons; oligo.; astro.; microglia
f Pv+, Sst+, Vip+ neurons
g Various glutamatergic, GABAergic, dopaminergic, and cholinergic neurons; astrocytes; oligodendrocytes
h Neurons, other cells

Table 1. This table provides a comparison of the mapping methodologies of different papers. Green indicates, for the first two columns, a wide breath of coverage in either various cell types or spatial extent in neural space; for the third column, green indicates whether the maps were quantitative, providing cell counts or absolute densities. Magenta indicates a lack of breadth in coverage in terms of specific cell types being mapped or in terms of spatial extent across mapped across the mouse brain. In the third column, magenta indicates a lack of cell count or common unit density information. MISS provides quantification of a large number of different types of cells, and in particular different types of neurons, across the entire mouse brain, at a small mesoscale resolution per voxel, of absolute cell counts and densities, getting around the tradeoffs of prior work quantifying and mapping many different types of cells across the whole brain. Our estimates are achieved without the need for computationally expensive and time-consuming cell counting as we employ matrix inversion using only genetic expression metadata between ISH and scRNAseq datasets.

RESULTS

Overview of Matrix Inversion with Subset Selection (MISS)

A schematic of the MISS pipeline is displayed in **Figure 1**. We extracted publicly available *in situ* hybridization[20] and single-cell RNAseq data[6,21] and collected all overlapping genes between the two datasets (**Figure 1a**), resulting in a dataset that comprises $N_V = 50246$ voxels, $N_G = 3855$ shared genes, and $N_T = 25$ neuronal and non-neuronal cell types. Since non-specific genes can potentially cause noise and artifacts, we tested several algorithms for gene subset selection (**Figure 1b, Table 2**). We then solve a matrix inversion problem to find cell type density per voxel, extending Grange *et al*[17], and apply a global scaling factor informed by the literature[3] to yield absolute counts per voxel per cell type (see **Figure 1c** and **Methods**). All selection methods and algorithmic choices were evaluated against various goodness-of-fit (GOF) metrics enumerated in **Table 2**, especially the combined GOF metric Σ_{fit}.

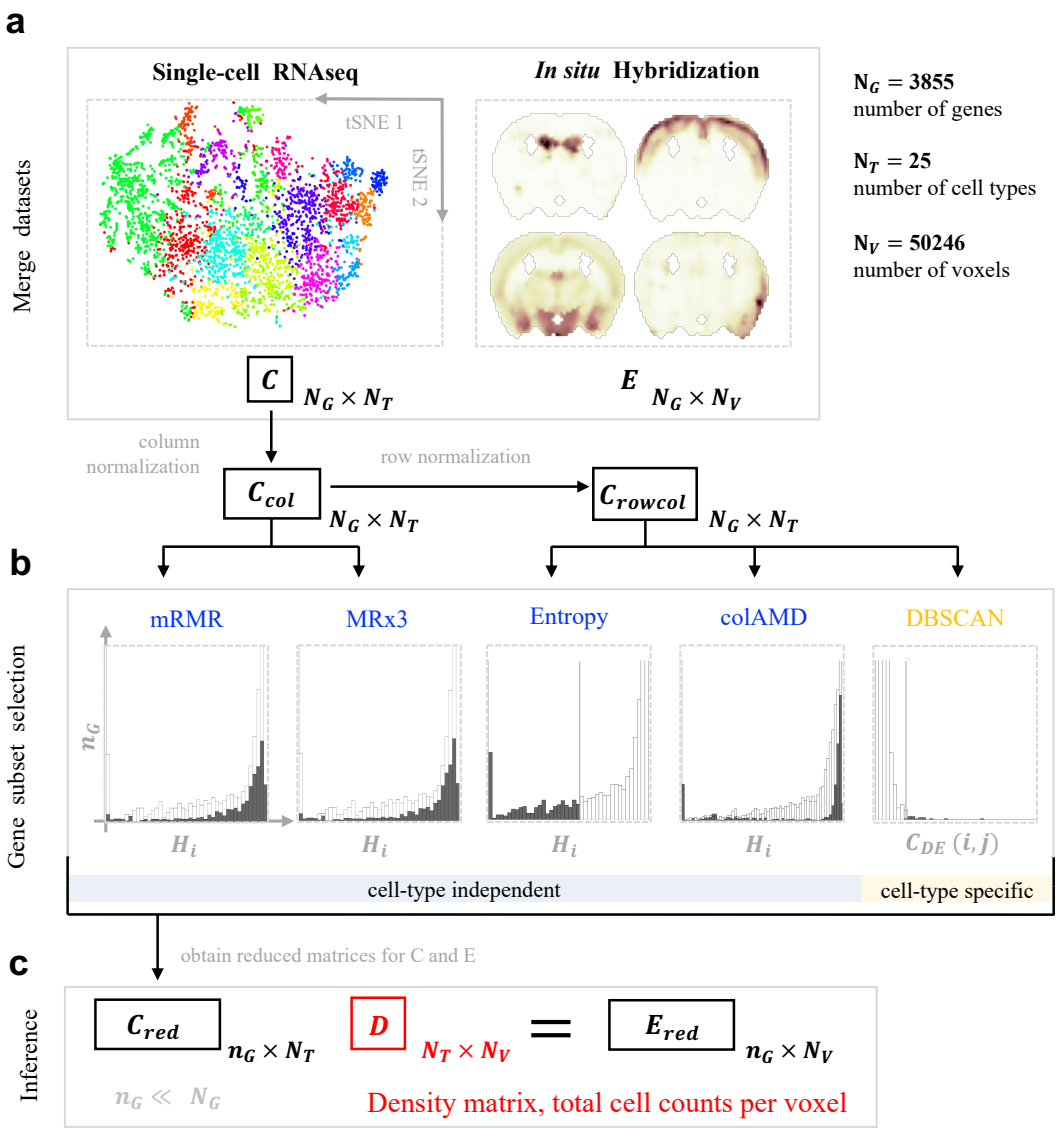

Figure 1: Overview of the workflow used in this paper for inferring cell counts. (a) We first extracted publicly available *in situ* hybridization[20] and single-cell RNAseq data[6,21]. After determining the intersection in gene space between the two datasets and performing subset selection to remove uninformative genes, we solve a matrix inversion problem to find the cell type density per voxel, D, following Grange *et al*[17]. We then apply a global scaling factor extracted from the literature[3] to determine an estimate of counts per voxel across all cell types in C_{red}. (b) We tested five different subset selection methods, which act on either C_{col} or C_{rowcol} and operate either on the columns (cell types) individually or on all of C, as shown in the flow chart. The histograms depict how the selected genes (approximately 500 in each method) distribute in either entropy (H) or C_{rowcol} space relative to the unselected genes, with vertical lines indicating the threshold used if the method imposes a hard threshold in either of these spaces. (c) We infer the density per cell type across all voxels of the mouse brain using the n_G genes determined by subset selection. Refer to **Methods** for more details.

Goodness-of-fit Metric	Description
τ_{adj}	A modified Kendall's τ rank correlation between the observed ordering of average distances to the cortical surface for seven layer-specific neocortical glutamatergic neurons and the expected ordering based on their given labels[6]. The raw correlation is down-corrected for insufficient and off-target (i.e. non-neocortical) signal.
R_c	The Lin's concordance correlation coefficient[55] between regional cell count estimates inferred with MISS and corresponding literature-derived values, which estimates the goodness-of-fit relative to the line $y = x$.
Σ_{fit}	A holistic measure combining R_c values for four distinct cell types and the glutamatergic layer-ordering metric τ_{adj} $\Sigma_{fit} = R_c(PV) + R_c(SST) + R_c(VIP) + R_c(microglia) + \tau_{adj}$
Subset Selection Method	**Description**
Entropy	All rows (genes) of C_{rowcol} with entropy scores *lower* than a given threshold are selected.
colAMD	The first n_G rows are selected after permuting the rows of C_{rowcol} according to the column approximate minimum degree algorithm[53].
DBSCAN	All genes that are determined to be "outliers" after applying the DBSCAN radial clustering algorithm[54] on each column of C_{rowcol} are selected.
mRMR	The Maximum Relevance – Minimum Redundancy algorithm[18] selects genes in an iterative, greedy fashion according to a criterion that weighs the between-cell-type variance of each row of C_{col} and its mean similarity to genes already selected.
MRx3	The Maximum Relevance – Minimum Redundancy – Minimum Residual algorithm uses the mRMR framework but adds a penalty term to the selection criterion accounting for the estimated projection error added by including a given gene.

Table 2. Definitions of the various goodness-of-fit metrics utilized by MISS and the five subset selection methods tested for the purposes of gene selection; see **Methods** for complete descriptions.

MRx3 provides the best overall performance among subsetting methods for MISS

To test the hypothesis that gene subset selection can markedly improve cell count inference, we implemented and evaluated five selection algorithms (**Table 2**). As anticipated, there is a wide variance amongst GOF metrics across subsetting methods and the range of n_G values (**Figures 2a-c**). However, MISS performance was consistently suboptimal using the full complement of genes (rightmost n_G value in **Figures 2a-c**). These quantitative GOF results mirrored qualitative assessment of the resulting maps; for instance, **Figure 2d** shows coronal sections of inferred density of two different layer-specific glutamatergic neurons. Notably, using all available genes (or too few genes) results in maps that are more diffuse and in some cases less patterned compared to the optimally tuned and subset-selected model results, outlined in red. Thus, gene subset selection is a necessary component of MISS.

Of the five subsetting methods, our novel MRx3 method exhibited the best overall performance on the combined GOF Σ_{fit} at $n_G = 540$, constituting ~14% of all available genes (**Figure 2a, S. Figures 1,2**). In particular, it exceeded the performance of the unmodified mRMR method. This optimum is primarily undergirded by MRx3's unique success at recapitulating literature estimates of Pv+ and Vip+ interneurons at $n_G = 540$ (**Figure 2c**, panels 1,3); however, performance is excellent for this gene subset for the layer-ordering metric τ_{adj} (**Figure 2b**) and the remaining two cell types as well (**Figure 2c**, panels 2,4). Further, the banding patterns of L5-IT and L6-CT in the neocortex are sharp and distinct, whereas there is visibly less sensitivity and specificity at non-optimal values of n_G (**Figure 2d**). We therefore conclude that Σ_{fit} is a reasonable holistic GOF measure and that MRx3 at $n_G = 540$ yields optimal cell count estimates. <u>Unless otherwise noted, results presented below were obtained using this optimal gene subset</u>.

Next we examine the quantitative concordance of MISS against literature-derived cell counts, using studies listed in **Table 1**, with the addition of total neurons[22] and total cells[3] – see scatter plot in **Figure 2e**. MISS achieved excellent overall concordance between the predicted cell counts per region and those measured by single-cell counting methods (R_c=0.69), and compares favorably to a previous computational approach to derive cell counts[5]. Additionally, the similarity between R and R_c shows that there is no global bias in our methodology. Much of the disagreement between our method and the literature lies outside of neocortical regions (green), and especially in midbrain and hindbrain (blue). This is expected since the scRNAseq data used here did not sample cells from the latter regions. Despite this variance, the global agreement suggests that our computationally inexpensive matrix inversion method faithfully reproduces cell counts across the whole brain.

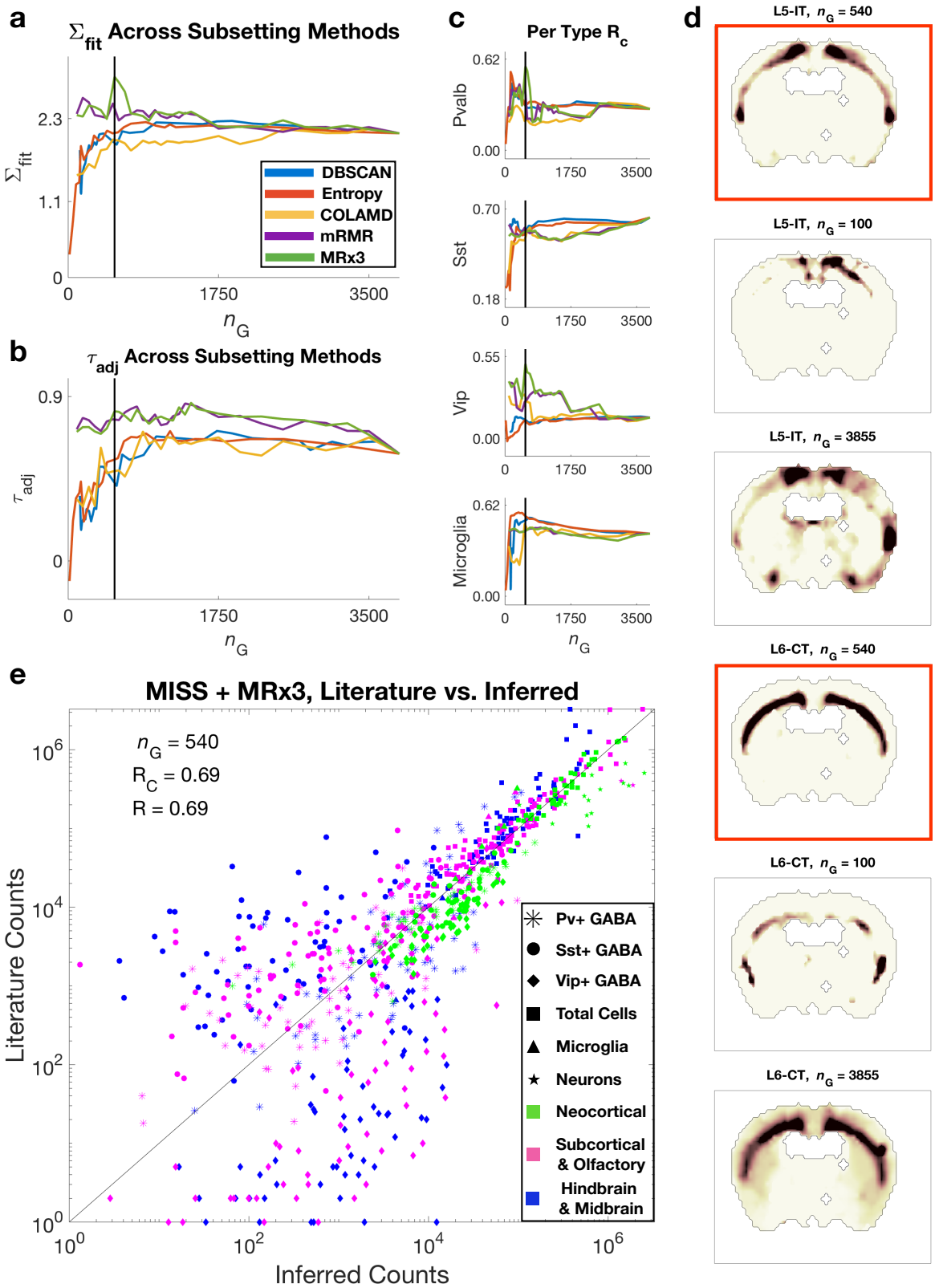
a
Σ_{fit} Across Subsetting Methods
Σ_{fit}
2.3
1.1
0
0
1750
3500
n_G
DBSCAN
Entropy
COLAMD
mRMR
MRx3
b
τ_{adj} Across Subsetting Methods
τ_{adj}
0.9
0
0
1750
3500
n_G
c
Per Type R_c
Pvalb
0.62
0.00
Sst
0.70
0.18
Vip
0.55
0.00
Microglia
0.62
0.00
0
1750
3500
n_G
d
L5-IT, n_G = 540
L5-IT, n_G = 100
L5-IT, n_G = 3855
L6-CT, n_G = 540
L6-CT, n_G = 100
L6-CT, n_G = 3855
e
MISS + MRx3, Literature vs. Inferred
n_G = 540
R_C = 0.69
R = 0.69
Literature Counts
Inferred Counts
10^0
10^2
10^4
10^6
Pv+ GABA
Sst+ GABA
Vip+ GABA
Total Cells
Microglia
Neurons
Neocortical
Subcortical & Olfactory
Hindbrain & Midbrain

Figure 2: Subset selection using MRx3 outperforms both other subset selection methods and performing matrix inversion using the full suite of genes. (a) Σ_{fit} is maximized by subsetting to 540 genes using MRx3. All subsetting methods except colLAMD produce a peak that outperforms using the entire suite of genes. (b) Only DBSCAN matches MRx3 in reproducing neocortical layer orderings assessed via τ_{adj}. All subset selection methods produce peak τ_{adj} values that are higher than those found using all the genes for matrix inversion. (c) R_c values between literature obtained and our inferred cell counts across individual cell types are either maximized by a large margin (Pv+ and Vip+ GABAergic interneurons) or are close to maximized (microglia and Sst+ GABA neurons) by MRx3. All cell types using all subsetting methods except colAMD produce maximum R_c values at a subset of genes smaller than the entire set. (d) Coronal slices from the middle of the brain comparing optimal subset selection, small subset selection, and no subset selection for inferring cell type maps, with L6-CT neurons used as an example. (e) The R_c value for all cell types with prior quantification across brain regions and our inferred counts obtained using 540 genes selected via MRx3 is strong and matches the Pearson's R value. Importantly, this means that the best-fit line is approximately $y = x$, indicting no global bias in how MISS infers cell counts.

Brain-wide maps of interneurons agree with experimental results

Figure 3a shows the optimal MISS results for Pv+, Sst+, and Vip+ interneurons side-by-side with corresponding maps produced using viral labeling[23]. Although these viral-labeled maps only include interneurons with monosynaptic inputs from the prelimbic (green) and infralimbic (red) areas, there is very strong visual agreement between experimental and MISS-inferred maps (**Figure 3a**). Concordantly, we achieve impressive quantitative agreement with prior work[1] across the whole brain, with $R_C \geq 0.50$ for all three interneuron types (**Figure 3b**). This agreement is especially notable since Pv+ and Sst+ neurons quantified outside the forebrain may not be the same cells as neocortex-extracted interneurons in the present dataset[6,21], accounting for our systemic underprediction, relative to data, of these cell types in midbrain and hindbrain regions (blue).

As expected from our maps (**Figure 3a**), we observed the highest overall interneuron densities in the neocortex, but the normalized ratios of Pv+, Sst+, and Vip+ interneurons were not constant (**Figure 3c**). In particular, Sst+ density was greater than that of Pv+ in the majority of neocortical areas, with Pv+ dominating primarily in the somatosensory areas (**Figure 3c**), consistent with previous findings[1]. Building on prior research suggesting spatial opposition between Pv+ and Sst+ GABAergic interneuron densities among neocortical regions[1], we explicitly demonstrate a strong negative correlation (**Figure 3d**), $R = -0.57$, $p < 0.001$. No significant or strong relationship exists between the neocortical distributions of either Pv+ or Sst+ and Vip+ cells (**Figure 3d**).

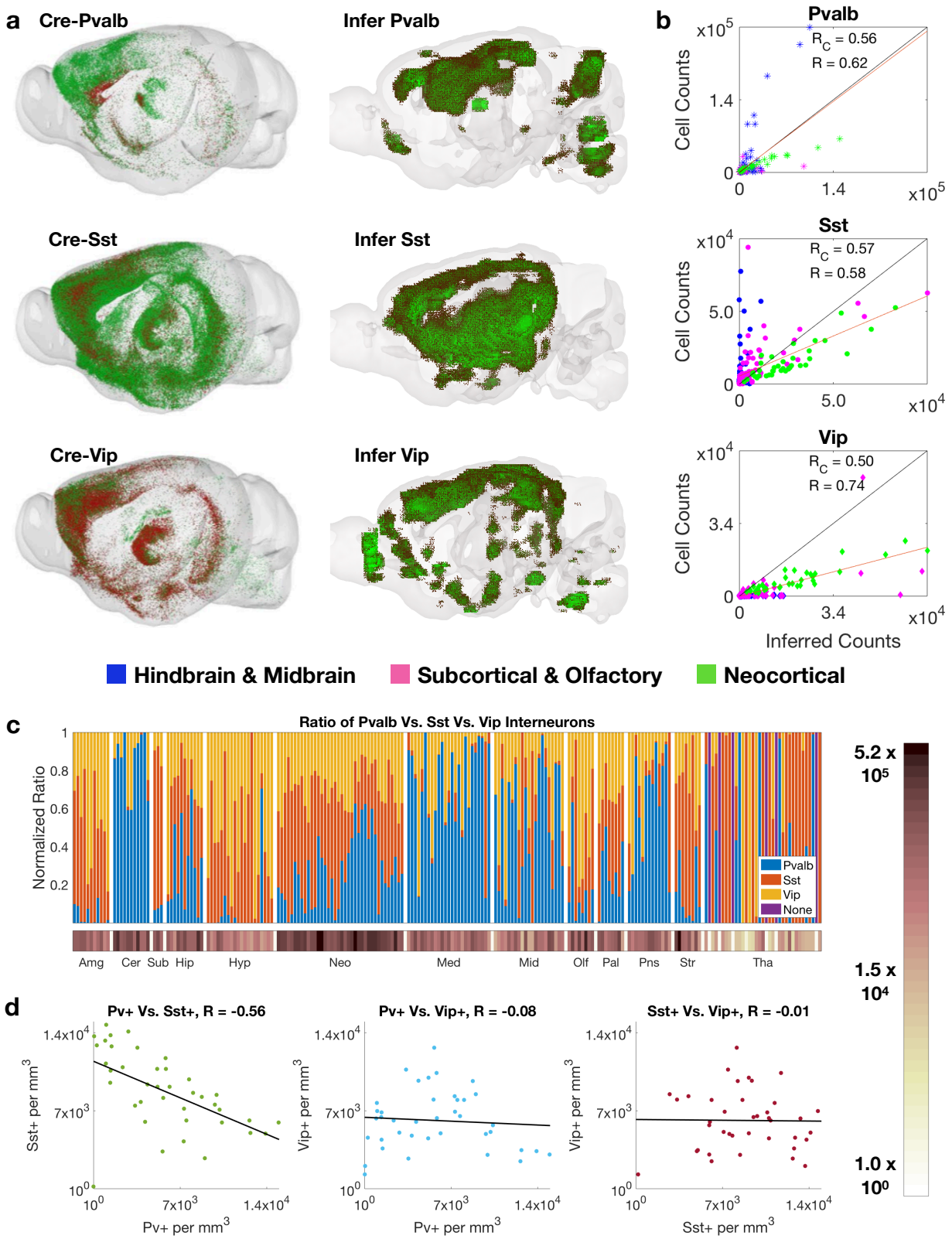
a
Cre-Pvalb
Infer Pvalb
Cre-Sst
Infer Sst
Cre-Vip
Infer Vip
b
Pvalb
R_C = 0.56
R = 0.62
Sst
R_C = 0.57
R = 0.58
Vip
R_C = 0.50
R = 0.74
Cell Counts
Inferred Counts
Hindbrain & Midbrain
Subcortical & Olfactory
Neocortical
c
Ratio of Pvalb Vs. Sst Vs. Vip Interneurons
Normalized Ratio
Pvalb
Sst
Vip
None
Amg
Cer
Sub
Hip
Hyp
Neo
Med
Mid
Olf
Pal
Pns
Str
Tha
5.2 x 10^5
1.5 x 10^4
1.0 x 10^0
d
Pv+ Vs. Sst+, R = -0.56
Pv+ Vs. Vip+, R = -0.08
Sst+ Vs. Vip+, R = -0.01
Sst+ per mm^3
Vip+ per mm^3
Pv+ per mm^3

Figure 3. Pv+, Sst+, and Vip+ GABAergic interneuron distributions are accurately inferred using MISS. (a) *Cre-Pvalb*, *Cre-Sst*, and *Cre-Vip* maps of interneurons connected to major long-range projecting subcortical nuclei[23] visually agree with our inferred maps of Pv+, Sst+, and Vip+ GABAergic interneurons. (b) The visual results in (a) are underscored by R_c values and R values consistently ≥ 0.50 as compared with regionally quantified counts of these interneurons from Kim, *et al*[1]. Importantly, most of the off-target estimates from MISS as compared with Kim occur in the hindbrain and midbrain, regions which Kim notes may include cell types that are not interneurons. (c) GABAergic interneurons are densest in the neocortex, hippocampus, striatum, cerebellum, and olfactory areas (heatmap bar at bottom). Relative densities of Pv+, Sst+ GABAergic interneurons show a kind of spatial opposition in the distribution of Pv+ interneurons as compared with Vip+ and especially Sst+ interneurons on a per region basis. (d) We demonstrate this spatial opposition cited above as Pv+ and Sst+ interneurons are explicitly inversely correlated within the neocortex.

Layer-specific cell type distributions reproduce neocortex laminar architecture

We next explored the layer-ordering metric, τ_{adj}, in more detail. Overall τ_{adj} is 0.82 at using the 540-gene subset from MRx3 (**Figure 4a**), with strong agreement throughout the neocortex. A qualitative assessment finds that Layer-2/3 neurons inferred by MISS are most enriched in a band just barely inside of and tracing the cortical surface while Layer-6 neuron enrichment forms a band that traces the interior border between the neocortex and white matter tracts, demarcated by ventricles. Layer-4 and Layer-5 neurons show enrichment in bands that are intermediary between Layer-2/3 and Layer-6 neurons, in the expected order (**Figure 4b**). Three-dimensional reconstructions of layer-specific glutamatergic neurons (**Figure 4c and 4d, S. Figure 4**) reinforce the per-slice results and provide a more comprehensive view of their whole-brain distributions. As expected of these cell types, they almost exclusively reside in their respective layers of the neocortex.

Ratio of Excitatory to inhibitory cells shows a bimodal distribution across regions

The proportion of glutamatergic versus GABAergic neurons exhibits marked variation between major region groupings, such as the neocortex or amygdala, while it tends to be similar in subregions within major regions (**Figure 4e**). Notably, the neocortex, thalamus, and hippocampus are predominantly glutamatergic (average glutamatergic fraction ~ 0.6—0.8), while most other major regions, including the amygdala and striatum, are mainly GABAergic (fraction ~0.2—0.3). We demonstrate brain regions can be divided into two distinct super-groups, which are responsible for the appearance of a distinct bimodal distribution of the glutamatergic fraction (**Figure 4f**). We expand on the implications of these findings in **Discussion**.

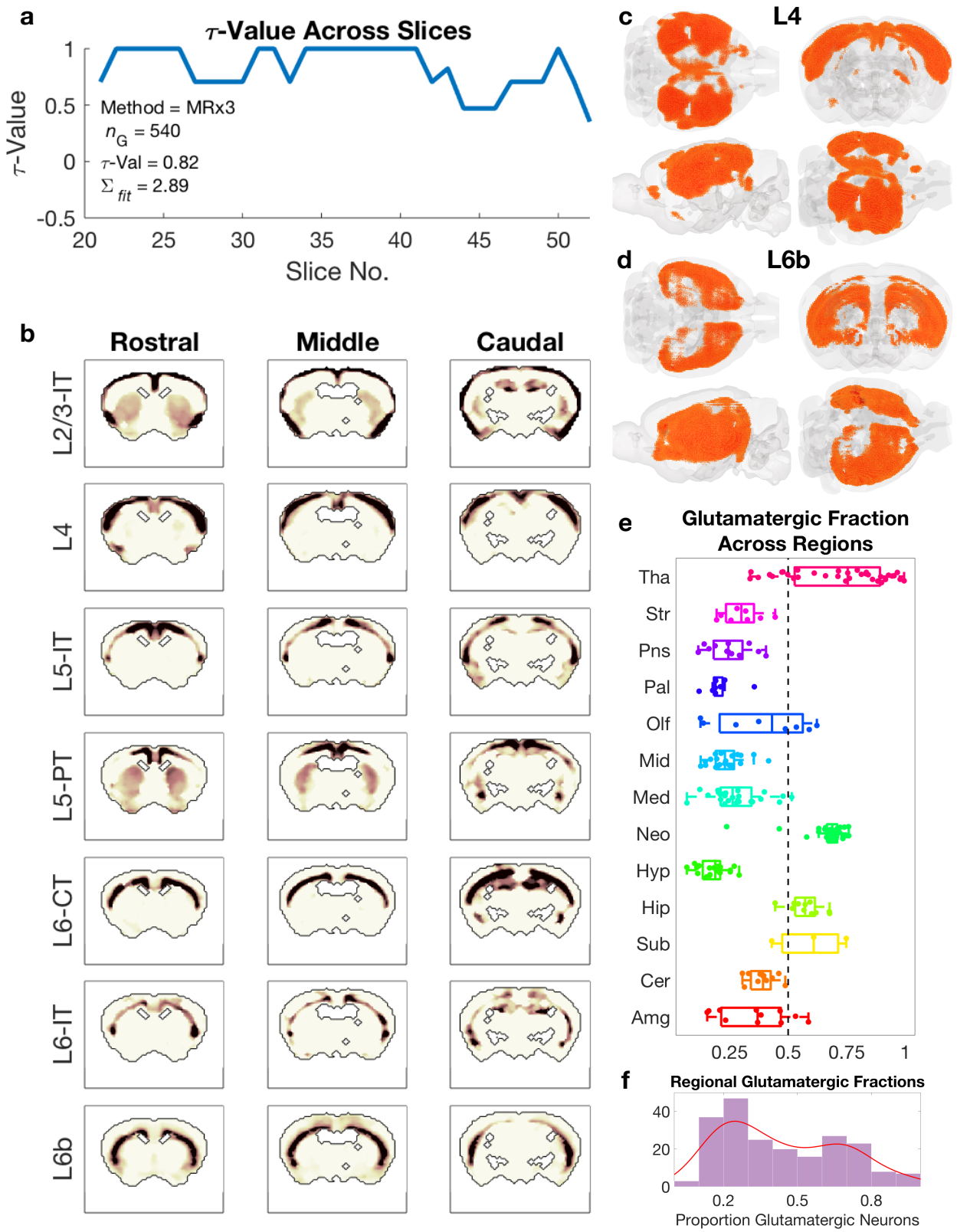
a
τ-Value Across Slices
τ-Value
Method = MRx3
n_G = 540
τ-Val = 0.82
Σ_{fit} = 2.89
Slice No.
b
Rostral
Middle
Caudal
L2/3-IT
L4
L5-IT
L5-PT
L6-CT
L6-IT
L6b
c
L4
d
L6b
e
Glutamatergic Fraction Across Regions
Tha
Str
Pns
Pal
Olf
Mid
Med
Neo
Hyp
Hip
Sub
Cer
Amg
0.25
0.5
0.75
1
f
Regional Glutamatergic Fractions
Proportion Glutamatergic Neurons

Figure 4. Laminar neocortical glutamatergic neuron distributions follow expected patterns while outside of thalamus, neocortex, and hippocampus, brain regions have fewer glutamatergic than GABAergic neurons. (a) Using MRx3 to select 540 genes for matrix inversion, MISS cell count inferences for laminar glutamatergic cells faithfully recreate neocortical layer structures across slices as assessed by τ_{adj}. (b) Inferred distribution of neocortical laminar glutamatergic cells recreate neocortical layers in slices taken rostrally, caudally, and in the middle of the mouse brain. (c & d) The laminar distributions are apparent not just in slices, but in 3D across the whole mouse brain volume; note the larger offset relative to the cortical surface and midline in L6b (d) neurons relative to L4 (c) neurons. (e) The thalamus, neocortex, and hippocampus are all composed off majority glutamatergic neurons, according to our inference maps using MISS, but the rest of the brain is dominated by GABAergic neurons. (f) We explicitly demonstrate that glutamatergic fraction across brain regions is a bimodal distribution, with a larger mode showing GABAergic predominance, and a smaller mode exhibiting a majority glutamatergic neuron fraction.

Glial cells have whole-brain distributions reflective of their biological roles

Of the three glial cell types within the scRNAseq dataset, current literature has precise quantification across regions only for microglia[19], whose agreement with MISS estimate is strong, with R_c = 0.43 (**Figure 5a**); three-dimensional reconstructions of microglial density are shown in **Figure 5b**. However, despite the paucity of whole-brain data[19], non-neuronal cell types also generally conformed to *a priori* expectations regarding their spatial distributions given knowledge of their functions. Astrocytes, the glial cells supporting the metabolic functions of neurons as well as synaptic transmission[24] are most concentrated in regions of the cerebellum, the site of heaviest gray matter concentration in mammals[19,25] (**Figure 5c**). Given the relatively high density of neurons in the cerebellum and the integral support roles astrocytes play, it may be expected that astrocyte density is most pronounced in the cerebellum as well. Meanwhile, oligodendrocytes, a glial cell type important for maintaining axon myelination[26], expectedly localize near major white matter tracts such as the fornix and corpus callosum and have a marked enrichment in ventromedial regions of the brain (**Figure 5d**); indeed, at the sub-millimeter resolution afforded by the ISH atlas, the corpus callosum is clearly delineated (arrows). Overall, the above results indicate that voxel-level MISS maps of neuronal and non-neuronal cells agree quantitatively with literature estimates where they exist, and qualitatively with their expected localizations given their specialized roles.

Adult cell type distributions and developmental ontology

Hierarchical clustering of regions by overall cell-type composition (**Figure 6a**) reveals a strong spatial pattern of cell type clusters that appear to be nonrandom supersets of the ABI adult mouse ontology. This is particularly evident in the first split, highlighted in the dendrogram in **Figure 6a**, as almost all thalamic regions, and only thalamic regions (pink), split off from the rest of the forebrain, mirroring the split of the diencephalon and telencephalon[27]. Given this observation, we sought to determine whether splits in developmental ontology reflect clusters of regions based on cell-type composition. We therefore compare clusters based on MISS-inferred cell type maps with empirical developmental groupings of brain regions from the ABI developmental atlas (see **Methods**) to test the hypothesis that regional developmental lineage persistently sets regional cell-type composition and cell type locations[2,27] into adulthood. Because the timing of the splitting within the forebrain and hindbrain is largely independent after they separate from each other[27], we chose to test our hypothesis in the forebrain and hindbrain separately, using separate hierarchical clusterings; all midbrain/hindbrain results can be found in **S. Figure 5**.

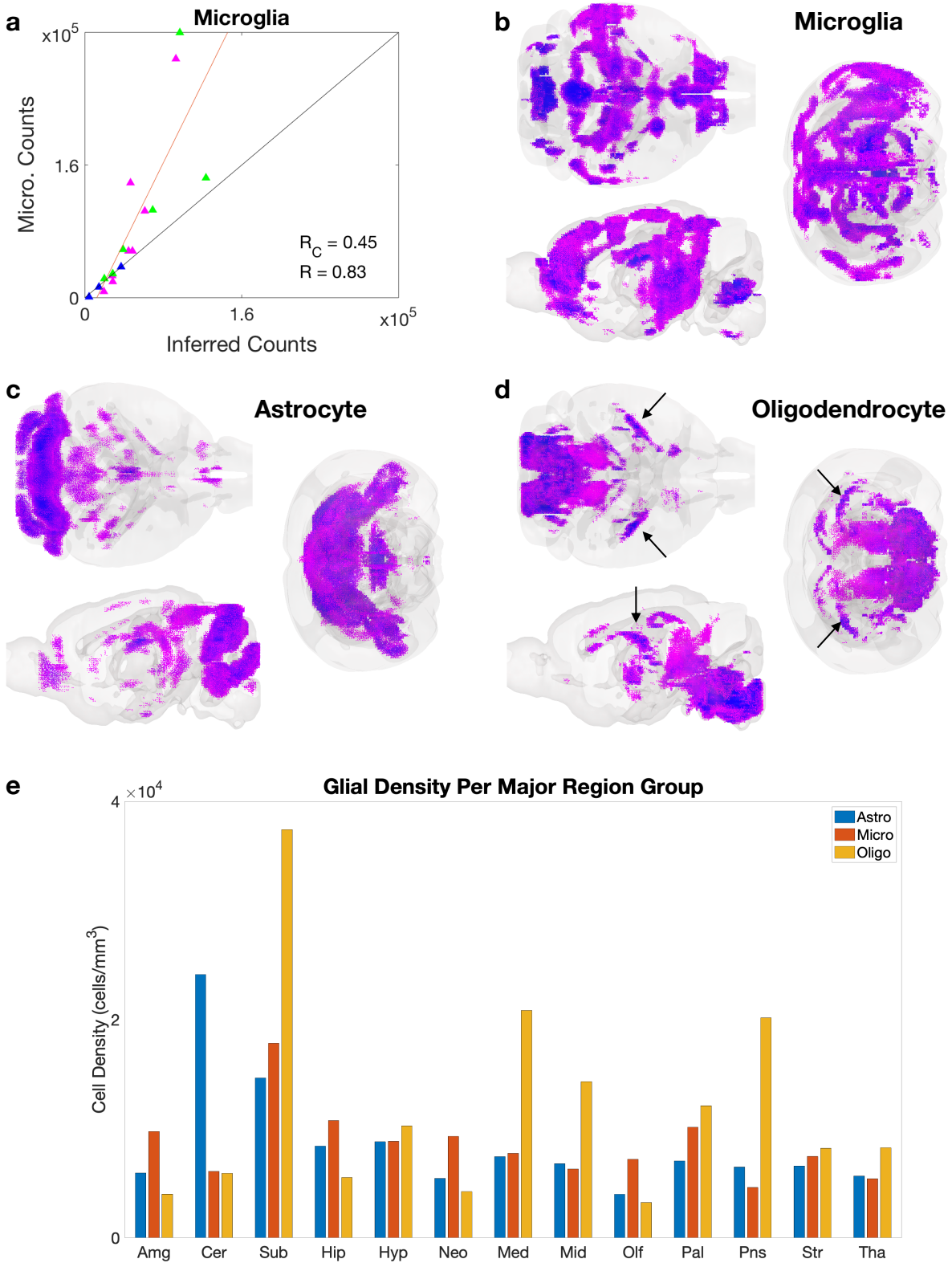
a
Microglia
x10^5
1.6
0
Micro. Counts
0
1.6
x10^5
Inferred Counts
R_C = 0.45
R = 0.83
b
Microglia
c
Astrocyte
d
Oligodendrocyte
e
Glial Density Per Major Region Group
×10^4
4
2
0
Cell Density (cells/mm^3)
Astro
Micro
Oligo
Amg
Cer
Sub
Hip
Hyp
Neo
Med
Mid
Olf
Pal
Pns
Str
Tha

Figure 5. Glial distributions either quantitatively reflect literature reported distributions or conform to a priori expectations regarding likely cell distribution across the brain volume given each glial cell type's biological role. (a) Microglial distributions inferred using MISS concord with literature values on the distribution of microglia, despite being slightly systemically under predicted; however, the R-value of 0.83 indicates strong concordance in terms of the (b) spatial pattern of microglial distribution as inferred and mapped using MISS. (c) Astrocytes are most concentrated in the cerebellum, subplate of the cortex, and hippocampus, in that order; these are generally considered regions of very high neuronal density. (d) Oligodendrocytes cluster near the midline more caudally and trace out the major white matter tracts of the corpus callosum (arrows) and fornix more rostrally. (e) Glial densities across major division of groups of brain regions conform to a priori expectations. As noted in (c), astrocytes are most concentrated in areas considered to have particularly high neuronal density and the high density of oligodendrocytes in the subplate of the cortex likely reflects the immediate proximity of that region to the major white matter tracts of the corpus callosum and fornix.

To quantitatively assess the concordance between regional hierarchical clustering and the developmental ontology (**Figure 6a**), we calculated (see **Methods**) the adjusted Rand index (ARI), which quantifies the pairwise overlap between categorical variables with arbitrary cluster numbers of any size distribution (the sample Rand index) relative to a null distribution. Analogous to R^2 in regression models[28], ARI can be interpreted as the portion of the variance explained between two clusterings beyond what is expected by chance. MISS using MRx3, across values of n_G, generally produces high mean ARI values against developmental ontology across the five tested sets of clusters (**Figure 6b**). At the optimal n_G=540, ARI is highly significant, many standard deviations above the mean RI of the null distribution for all five developmental splits, with a mean ARI value of 0.46 (**Figure 6c**). The significance of this correspondence is immediately apparent when directly comparing the RI null distributions (**Figure 6d**, blue histograms) to the RI between our regional clustering by cell-type composition and the developmental splits of the forebrain. These quantitative results are mirrored qualitatively in the "glass brain" renderings (**Figure 6d**) of the developmental ontology clusters alongside our cell-type composition clusters, with each forebrain region represented by a point-cloud sphere colored by cluster identity. There is strong visual agreement between the spatial distributions of inferred and developmental brain region clusters, particularly at $k = 2$ and $k = 5$, the cluster numbers with the highest ARI values. In contrast to the forebrain, clusters of midbrain and hindbrain regions overlapped no better than chance with ontology at any level of division (**S. Figure 5**), probably due to a lack of such regions sampled in the scRNAseq data. Overall, these data support the hypothesis that adult regional cell-type compositions and the spatial distributions of different cell types are largely set during neural development.

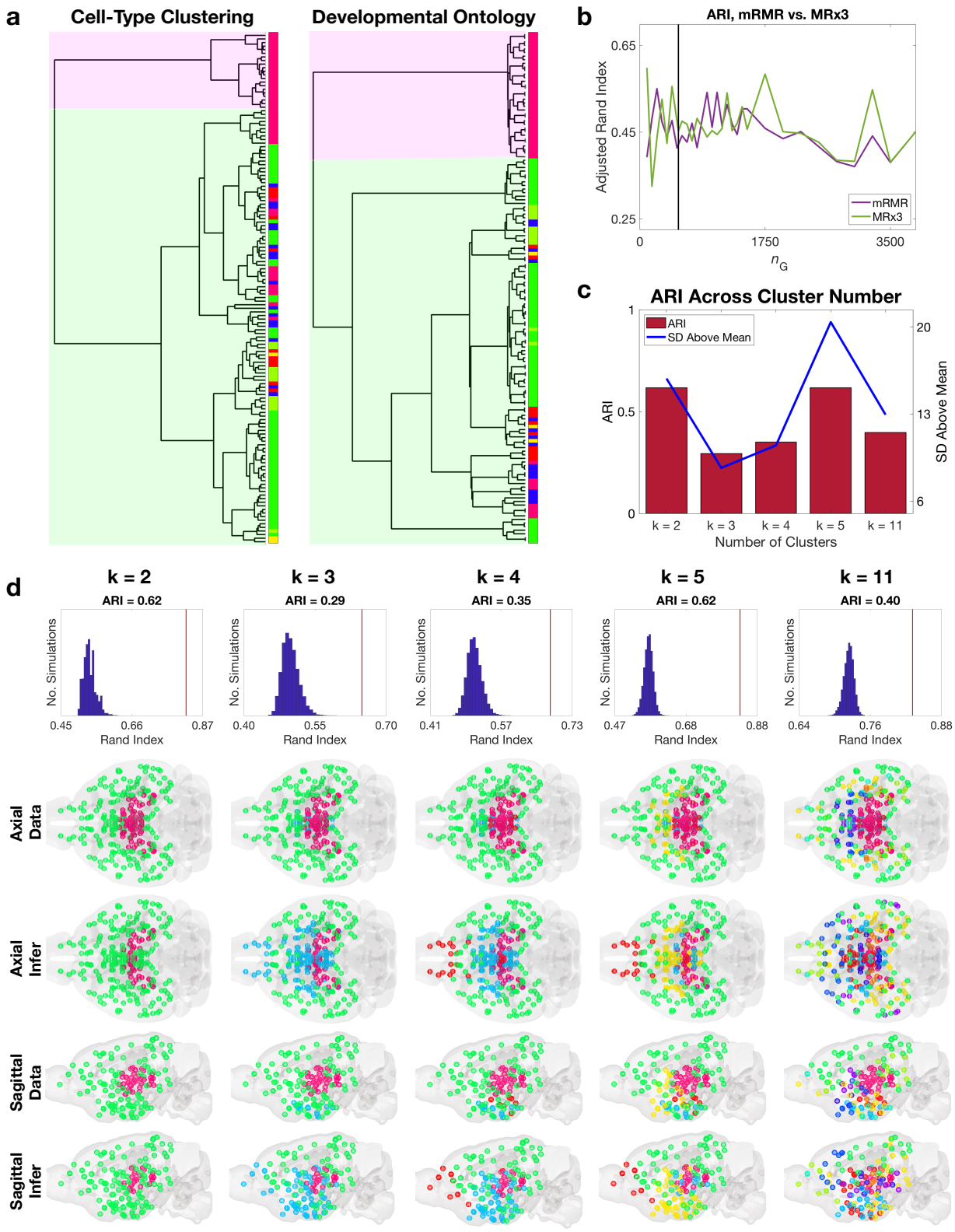
a
Cell-Type Clustering
Developmental Ontology
b
ARI, mRMR vs. MRx3
Adjusted Rand Index
0.65
0.45
0.25
0
1750
3500
n_G
mRMR
MRx3
c
ARI Across Cluster Number
ARI
SD Above Mean
1
0.5
0
20
13
6
k = 2
k = 3
k = 4
k = 5
k = 11
Number of Clusters
d
k = 2
ARI = 0.62
k = 3
ARI = 0.29
k = 4
ARI = 0.35
k = 5
ARI = 0.62
k = 11
ARI = 0.40
No. Simulations
0.45
0.66
0.87
0.40
0.55
0.70
0.41
0.57
0.73
0.47
0.68
0.88
0.64
0.76
0.88
Rand Index
Axial Data
Axial Infer
Sagittal Data
Sagittal Infer

Figure 6. ARI indicates high concordance between regions clustered by cell-type composition inferred using a subset of genes identified via mRMR and the developmental splits of the forebrain according to the ABI's developmental atlas. (a) Hierarchical clustering of brain regions from inferred cell-type densities exhibits a strong spatial component; in particular the thalamus splits from the rest of the forebrain as the first branch point (magenta versus green background), akin to the split of diencephalon and telencephalon. (b) MRx3 outperforms mRMR in ARI per parameter value averaged across developmental splits/*k* cluster numbers, perhaps indicating better overall cell-type performance. (c) ARI and SDs above mean random clustering RIs are highest at $k = 2$ clusters, as the thalamus neatly splits from the rest of the forebrain. Performance is strong across all k cluster numbers, however, and partially recovers at the highest cluster numbers of $k = 5$ and $k = 11$. (d) Our inferred regional cell-type compositions (red line) greatly outperforms randomly clustered regions (blue distribution) at producing a concordant clustering with regions grouped by ABI developmental ontology across all *k* cluster numbers. We observe strong visual concordance in 3D mouse brain renderings between brain regions clustered by cell-type (Infer) and ABI developmental ontology (Data).

DISCUSSION

Summary of key results

We provide a novel method to accurately infer the density of a diverse range of neuronal and non-neuronal cell types across the entire mouse brain at a sub-millimeter scale, even with very limited cell-type and spatial sampling. Three key methodological features make our results possible. First, we employ a computational pipeline, MISS, involving matrix inversion in order to project scRNAseq derived cell type features onto per-voxel ISH gene expression data (**Figure 1**). Second, MISS incorporates gene subset selection as a novel and essential preprocessing step, distinguishing it from previous approaches[17]. Third, we rigorously evaluated five feature selection algorithms, of which our novel MRx3 gave the highest performance (**Figure 2a-d**). Our inferred maps gave strong quantitative agreement with independent literature-derived regional estimates of GABAergic interneurons[1] (**Figure 3a**), microglia[19] (**Figure 5a**), total cells[3] (**S. Figure 3**), and total neurons[22] (**S. Figure 3**) and faithfully reproduce the laminar architecture of the neocortex (**Figure 4**).

Comparison to cell type quantification methods

MISS stands out from existing approaches for quantifying cell types because it bypasses the cell type specificity/spatial coverage tradeoff that has emerged in the field (**Table 1**). Previous attempts to quantify specific cell types across the whole brain at single-cell resolution have relied upon broad cell classes with at most two molecular markers[1,5,11–14]. Other groups have addressed this limitation directly and mapped hundreds of individual genes to achieve single-cell maps with an impressive depth of cell type coverage[4,7,8], but only for small fractions of the total mouse brain volume. Our approach, while compromising on single-cell spatial resolution, provides accurate quantification of a more detailed assortment of cell types than previous whole-brain mapping approaches; for many applications, determining cell counts at the resolution of the ISH atlas (200μm) is sufficient.

MISS can be performed quickly on a laptop, yielding cell counts registered to the mouse Common Coordinate Framework[29]. This portability is especially important as scRNAseq transcriptomic profiling data

become available for regions outside of the neocortex and thalamus, which MISS can easily accommodate to obtain maps of additional cell types. Alternative approaches that directly quantify cell types using fluorescence imaging, in addition to being limited in terms of their spatial coverage, require sophisticated and expensive microscopy platforms that may be inaccessible to many researchers looking to understand how cell types they identify transcriptomically are distributed throughout the brain[1,3,4,7,8].

Why is gene subset selection necessary?

Our results depend critically on the quality of gene subset selection. Without this step, the resulting maps become quantitatively inaccurate, with significant diffuse abundance patterns that are biologically implausible (**Figures 2a-d).** The issue is exacerbated by unsampled cell types in the ABI data used here[6,21], since a C matrix with missing cell types in **Equation 4** may potentially lead to error in the least-squares solution. Our subset selection step helps ensure that unsampled cell types do not appreciably contaminate the inference of sampled ones. Additionally, many genes are neither specific to the central nervous system, nor do they show appreciable gradients across the brain. The inclusion of such genes can lead to diffuse effects in inferred maps, since they simply add to the ill-conditioning of the matrix inversion without contributing any useful signal. However, we note that driving feature selection to an extreme, where only perfectly specific markers are retained, is also suboptimal. Very small n_G do not give good performance (**Figures 2a-d**), and there is apparent cross-specificity of many genes in the optimal MRx3-derived set (**S. Figure 2**), indicating that maximal performance is achieved at an intermediate subset of genes, whose identification is not trivial – an aspect that prior mappings using matrix inversion[17] have not addressed.

Biological implications of whole-brain neuron subtype distributions

Here we examine a few key biological implications of our cell type maps, focusing particularly on GABAergic interneurons and long-range glutamatergic neurons.

1) Pv+, Sst+, and Vip+ interneurons

Corroborating a prior characterization of whole brain distributions of Pv+, Sst+, and Vip+ interneurons[1], our inferred maps indicate that within the neocortex, Pv+ and Sst+ neurons are rarely present in comparable numbers within the same region. We expand on those prior results by demonstrating that Pv+ and Sst+ interneurons are strongly anti-correlated (**Figure 3d**). Furthermore, we find that outside of the neocortex (with the exception of the thalamus, which largely has negligible densities of these cell types), asymmetry between Pv+, Sst+ interneuron densities among major regions is very pronounced, with many major region groups containing predominantly one of these two interneuron subtypes (**Figure 3c**). Especially notable is a stark forebrain/hindbrain divide: we find strong Pv+ interneuron expression in midbrain and hindbrain regions, but Sst+ and Vip+ interneurons predominate in forebrain regions outside of the neocortex (**Figure 3c**). Exceptions to this general rule exist, particularly in the hippocampus where Pv+ interneurons are known to play an important role[30], but this divide carries implications for how intraregional signaling differs across the brain given well-characterized differences in spiking patterns between Pv+ and Sst+ interneurons[31]. Intriguingly, evolutionarily older brain structures largely lack Sst+ interneurons, hinting that this cell type may be newer in evolutionary age.

2) Glutamatergic neurons

Our inferred maps suggest that the predominant character of most region groups is inhibitory, with notable exceptions in the neocortex, hippocampus, and thalamus, whose high glutamatergic neuronal

densities may be reflective of the fact that these region groups in particular have numerous long-range, excitatory connections to other areas of the brain[29,32]. In the cases of the neocortex and hippocampus, relatively high glutamatergic densities may also reflect that within major-region mesoscale connectivity is often achieved by excitatory cell pairs, for example granule and pyramidal cell pairings in the hippocampus, and Layer-6 and Layer-4 neuron pairings in the neocortex[33,34]. More interestingly, proportions of glutamatergic versus GABAergic neurons displays a bimodal distribution (**Figure 4f**), with two peaks at 0.2–0.3 and 0.6–0.8 excitatory / (excitatory + inhibitory) cells. Furthermore, subregions belonging to the same larger region, such as the neocortex, amygdala, or hippocampus, almost universally possess similar glutamatergic neuron fractions (**Figure 4e**). Because the glutamatergic fractions of smaller brain regions within a major region generally agree, we posit the bimodal distribution of glutamatergic proportion may reflect an important branch point in functionality between brain regions. Although these results have to be interpreted carefully, they suggest that macroscale organizing principles differ between anatomical groups of regions but are largely shared within groups, perhaps reflecting important functional divisions between groups of brain regions.

Developmental origins of adult cell type distributions

A quantitatively accurate cell type mapping platform like MISS can potentiate rigorous testing of important but currently qualitative hypotheses. To demonstrate this we addressed a key neuroanatomic question: does hierarchical clustering of regions based on cell type composition (**Figure 6**) recapitulate the developmental ontology of the mouse brain? As prior work has hypothesized that regional developmental lineage helps set regional cell-type composition and cell type locations[2,27], comparing ABI region clustering based on our cell type mappings can simultaneously serve as a test of the accuracy of our maps as well as a quantitative assessment of the theory that cell type locations are largely set during neural development. Using the ABI developmental atlas, which is based on molecular patterning during development, we identified five distinct stages of splitting relative to the ABI brain segmentation for adult mice within the forebrain (see **Methods**). The ARI results presented in **Figure 6** constitute some of the first quantitative support for a strong putative persistence in the mouse forebrain of the spatial distribution of cell types from fetal to adult life stages. That is, even as groups of neural cells change their expression profiles over organismal life stages, their group membership and spatial locations remain constant, as distinct types of cells change together synchronously. Thus, the spatial distributions of different cell-types in the adult brain significantly correlates with the staging of developmental splits *in utero*.

If our maps were unrepresentative of whole-brain cell type distribution, a correspondence between hierarchical brain region clustering and developmental ontology would be virtually impossible due to chance (**Figure 6d**). Hence our ARI results provide additional quantitative validation to our maps. We note however that ARI is highest in forebrain regions and lower in midbrain and hindbrain regions (**Figure 6, S. Figure 5**), likely due to sparse number of neuromodulatory cells in the ABI data. With additional sampling of midbrain and hindbrain regions enriched in these unrepresented cell types we expect the correspondence with developmental ontology will improve.

Further Potential Applications

MISS can help address the extent to which cellular identities of brain regions governs the formation of synaptic connections[35] and inter-regional neural connectivity[36,37]. Questions surrounding whether certain behavioral, cognitive, or sensory processing abilities are correlated with certain cell types, their spatial distribution, or their location within connectivity networks[38–41], can also benefit from our maps. Clinically,

our maps could further understanding of the selective vulnerability of brain regions such as the entorhinal cortex to early tau inclusions in Alzheimer's Disease[42] or the substantia nigra pars compacta to early synuclein inclusions in Parkinson's Disease[43]. The spatially varying abundances of cell types considered selectively vulnerable to tau or synuclein inclusions can be mapped using MISS, and their correspondence with the spatial pattern of protein pathologies can be tested. While regional gene expression profiles did not seem especially predictive in a prior analysis[44], other experiments suggest cell type selectivity of tau pathology[45–47]. Cellular vulnerability in other neurological conditions can also be interrogated using MISS, including psychiatric diseases such as schizophrenia[48], and traumatic brain injury (TBI), which was hypothesized to preferentially involve certain types of cells in both injury and recovery phases[49,50]. These applications exemplify the broad scientific utility of whole-brain cell type quantification.

Method limitations

The most significant limitation is the restricted number of regions (neocortex and thalamus), and a notable absence of various classes of neuromodulatory neurons, in the ABI scRNAseq dataset. This is not a methodological but dataset limitation. Another drawback is the requirement for an empirical rescaling parameter to obtain cell counts per voxel, which is a consequence of ISH-based energy being derived from fluorescence intensity and not actual transcript counts[20]. We inferred a global scale factor based on the average neocortical cell density derived using CUBIC-X[3] (**Equation 3**), instead of type-specific factors, which we did not consider biologically justified. This methodological choice makes validating MISS estimates against independent literature values more challenging, as any discrepancies between CUBIC-X and its alternatives will be propagated to our results; this is particularly pronounced for our total neuronal count estimates (**S. Figure 3**). However, despite these limitations, the strength of our results as a whole indicates that we can accurately reproduce cell counts at per voxel resolution using MISS.

Conclusion

We propose a novel computational pipeline for high-accuracy cell count inference using ISH and scRNAseq data across the entire mouse brain. Our results demonstrate that verifiable quantification and mapping of neuronal and glial subpopulations with well-differentiated glutamatergic and GABAergic subpopulations can be obtained using relatively small numbers of cells and brain regions. We used the inferred maps to quantitatively explore the relationship between adult neural cell-type distributions and other macroscale neuroanatomic characteristics of mammalian nervous systems, especially their developmental ontology. The presented maps and computational pipeline can be used as an inexpensive alternative to single-cell counting for quantifying absolute numbers of more cell types than current whole-brain approaches can accommodate.

METHODS

Input datasets:

Input data for cell count inference were derived from publicly available murine datasets from the Allen Institute for Brain Science (ABI).

<u>Single-cell RNA sequencing:</u>

We utilized all currently available single-cell RNA sequencing (scRNAseq) data from the ABI website (http://celltypes.brain-map.org/rnaseq), consisting of 27477 individual cells isolated from three distinct brain regions (primary visual cortex (VISp), 15413 cells; anterior lateral motor cortex (ALM), 10068 cells; lateral geniculate complex (LGd); 1996 cells) profiled across 45768 unique genes. Cells were collected from five distinct mouse Cre lines for pan-neuronal coverage: (*Snap25-IRES2-Cre;Ai14),* glutamatergic (*Slc17a7-IRES2-Cre;Ai14*, neocortical; *Slc17a6-IRES2-Cre;Ai14*; subcortical) and GABAergic (*Gad2-IRES- Cre;Ai14*, *Slc32a1-IRES2-Cre;Ai14*). Cells isolated from neocortical areas were extracted using layer-enriching dissections (L1, L2/3, L4, L5, and L6), amplifying the relative abundance of neuronal cell types and providing spatial information to corroborate the assignment of glutamatergic cell types to specific layers. After sorting and isolating the live cells into individual wells using FACS, mRNA was extracted and amplified with RT-PCR. The resulting cDNA library was sequenced using Illumina HiSeq 2500 DNA sequencers, which produced single-end reads that were then aligned to the mm10 murine reference genome to quantify the presence of each transcript. The raw sequence counts per cell were stored in two data tables, one for alignments to exons and another for introns.

The cells in the database were then classified into unique clusters, which were taken to be distinct cell types, based on differential expression scores of a reduced set of differentially expressed genes. The authors implemented a multistep clustering pipeline that first utilizes two complementary dimensionality-reduction algorithms to reduce the sample space of the data, iterative principal component analysis (PCA) and iterative weighted gene co-expression network analysis (WGCNA), then clusters the resulting "modules" hierarchically using the Jaccard-Louvian method[51] or Ward's method, depending on the number of cells to be clustered. Branches of this hierarchical clustering tree were merged if they contained too few branches or were too similar to neighboring branches. The entire pipeline was repeated 100 times on random subsets of 80% of the cells to determine a consensus clustering. The resulting clusters were identified and validated using three sources of independent information: the layer-enriching dissection from which the cells were extracted, the presence of differential expression markers corresponding to known or newly discovered cell types, and the localization of these markers as determined by *in situ* hybridization. Based on these labels, the clusters were further grouped into a three-level hierarchy, representing broader classes of cell types that were of particular interest in the present study. The high robustness of this labeling and classification of cell types within this particular scRNAseq dataset allowed us to confidently determine whole-brain spatial patterns, since the cell type labels themselves were already validated. For further methodological details, see Tasic *et al*[6] and the RNAseq documentation on the ABI website (http://celltypes.brain-map.org/rnaseq).

The scRNAseq data exists as tables of raw exon and intron counts (sequence hits) separated by sample ID and by gene for three distinct brain regions. For each of these regions, we combined the raw exon and intron counts into a single metric according to ABI guidelines:

$$CPM_{ij} = log_2\left(10^6 \times \frac{exons_{ij} + introns_{ij}}{total_j} + 1\right)$$

where CPM_{ij} is the sample-normalized expression (in counts per million) of gene i in sample j and $total_j$ is the total number of reads for all genes in sample j. We then utilized the existing cluster identification for each sample (excluding those labeled "low quality", "doublet", or "outlier") to derive each gene's mean expression for the cell types previously determined in the ABI dataset[20]. For samples extracted from neocortical regions, we used the correlation coefficients between their individual expression and their

cluster's center-of-mass to infer a more accurate mean expression for the cluster; for samples from the lateral geniculate complex, no such information was available and an unweighted average was used instead. The resulting clusters, however, represent cell types that were too specific for our purposes, as we were interested in the spatial localization of the broader subclasses and classes of cell types (e.g. all Layer-5 pyramidal tract neurons as a single group). Some rarer types also contained very few individual cells. We therefore determined the expression of these broader cell type designations by averaging the expression of the clusters assigned to them, weighted by the number of samples per cluster; it has been previously shown that when cell types are combined in this way, under matrix-inversion approaches the resulting inferred counts represent a combined signal of the constituent cell types[17]. The resulting dataset contains genome-wide expression data for 21 neuronal and 4 non-neuronal cell types (**S. Tables 1 & 2**). More specifically, the following groups of cell types are represented: 1) neocortically derived, layer-specific glutamatergic neurons; 2) neocortically derived GABAergic interneurons (Pv+, Sst+, and Vip+); 3) four non-neuronal types (microglia, astrocytes, oligodendrocytes, endothelial), all derived from the neocortical and thalamic regions; and 4) various other glutamatergic and GABAergic neurons which were labeled with marker names we could not trace back to well-characterized cell types. Several of the non-neuronal cells represent a pooled signal between related, associated types because of the relative scarcity of these types in the dataset: "microglia" represents a combined signal across specific types of microglia and macrophages, "oligodendrocytes" represents a combined signal across specific types of oligodendrocytes and OPCs, and "endothelial" represents a combined signal across true endothelial cells, pericytes, SMCs, and other vasculature-related types.

In situ hybridization (ISH):

Our spatially realized expression data were derived from the publicly available ISH dataset published by the ABI (https://mouse.brain-map.org/search/index). We specifically utilized the coronal dataset, which contains better whole-brain coverage than the sagittal series, at the cost of less genomic coverage (4344 ISH probes covering 4083 unique transcripts). The brains of 56-day-old C57BL/6J mice were extracted and sectioned in 25-μm slices, which were separated out into 8 series of 56 slices each uniformly spaced 200-μm apart. Each riboprobe corresponded to one series and was designed to have minimal overlap with other transcripts to prevent signal contamination by off-target binding. Post incubation with the probe, slices were imaged in high resolution (1.07-μm pixels) and coregistered onto a common 3-dimensional space. The expression data were downsampled by averaging the grayscale intensity of expressing pixels within a 200-μm by 200-μm area and dividing by the total number of pixels in that area ("expression energy"), yielding a measure of gene expression over a rectangular volume of 67 by 41 by 58 voxels. For further details, see Lein *et al*[20] and the ISH documentation from the ABI (http://help.brain-map.org/display/mousebrain/Documentation). We normalized each gene's expression by its sum across all voxels, so that they were on comparable scales for cell count inference.

Ontology reference:

For our developmental ontology analysis (see **Parameter Optimization and Method Validation: Recreating ontological splits during neural development** below), we utilized the recent neural tube differentiation staging scheme developed by the ABI[27]. Briefly, the ABI developmental ontology describes the topographical relationships between brain regions in the context of the developing mouse brain at several time points, relying upon the expertise of the lab of Dr. Luis Puelles in embryonic molecular patterning.

Cell Count Inference:

Our overarching goal in this study was to obtain accurate counts for individual cell types across the whole mouse brain. Grange *et al* first introduced a mathematical framework for inferring voxel-wise cell type densities, which posits that ISH voxel energy for a given gene is proportional to each cell type's expression value for that gene multiplied by its density in that voxel, summed across all cell types within that voxel[17]. The original study relied upon microarrays for cell type-specific expression data limiting their ability to infer cell counts across the mouse brain despite achieving impressive density maps across 64 unique cell types[17]. By using scRNAseq instead of microarray data, besides being a more precise method of measuring gene expression, we can ensure that each cell type-specific expression profile is on the same absolute scale - that of a single cell of that type - facilitating precise quantification of cell counts per voxel.

We can generalize the relationship between expression energy per voxel and cell type-specific gene expression across all voxels and genes in matrix form as follows:

$$CD = E \tag{1}$$

where E is the row-normalized genes-by-voxels ($N_G \times N_V$) expression matrix extracted from the ISH data, C is the row-normalized genes-by-cell-types ($N_G \times N_T$) expression matrix extracted from the scRNAseq data, and D is a cell-types-by-voxels ($N_T \times N_V$) matrix of cell densities. To solve **Equation 1** the matrix E must be inverted in some manner; let us denote for convenience $C^{\#}$ a suitably defined pseudo-inverse of C. Hence we estimate

$$\widehat{D} = \gamma C^{\#} E \tag{2}$$

Since the entries of E are in arbitrary expression units, a global constant γ was introduced in order to convert inferred cell counts into quantitatively accurate units. This factor can be inferred from the literature. In practice, a classical Moore-Penrose pseudo-inverse of C is unsatisfactory since it does not enforce the biological fact that cell densities cannot be negative. Hence in this paper $\widehat{D}$ was estimated using the `lsqnonneg` function in MATLAB, a least-squares solver with a built-in non-negativity constraint:

$$\widetilde{D} = \underset{D, D_{ij} \geq 0 \ \forall i,j}{\arg\min} \|E - CD\|_F$$

where the matrix norm above is Frobenius. Then the final estimate is $\widehat{D} = \gamma \widetilde{D}$, with

$$\gamma = \frac{\rho_{neo}}{\sum_{k=1}^{N_V^{neo}} \sum_{j=1}^{N_t} \widetilde{D}(j,k)} \times V_{corr} \tag{3}$$

where ρ_{neo} = 127870 cells/mm^3 is the total cell density in the neocortex[3], $V_{corr} = \frac{(0.2mm)^3}{1mm^3}$ accounts for the difference in voxel size between the ISH expression atlas and density values, N_T is the number of cell types, and N_V^{neo} is the number of neocortical voxels. We chose this rescaling factor because we reasoned that our densities would be most accurate in the neocortex; note, however, that we scale all entries of D by this constant and it incorporates no cell type-specific information. We directly compared the resulting inferred

counts, summed across anatomical regions, to counts determined in several previously published studies, and derived novel metrics to further assess the accuracy of our mapping (See **Parameter Optimization and Method Validation** below).

Gene subset selection:

A fundamental limitation to the matrix inversion scheme (**Equation 1**) is that it implicitly assumes that the columns of C span all of the relevant cell types in all voxels across the brain. In our case, where we derive C from scRNAseq data obtained from only three distinct anatomical regions, this assumption is clearly violated. Furthermore, many genes carry only limited information in differentiating cell types represented in our dataset, and therefore only add noise to the system. Both of these problems can be ameliorated by performing the matrix inversion only over the set of maximally informative genes. This is done by removing rows of C and E corresponding to low-information genes and forming reduced-dimension versions: C_{red} and E_{red} (**Figure 1b**). Determining such a subset is a nontrivial optimization problem, and we tested several single-parameter methods to determine which produced the best cell type mapping across several performance metrics.

Normalization of C: Although the matrix inversion described above is performed on the matrix C, the gene selection step requires some normalization in order to remove the effect of experimentally-induced scale factors amongst genes and cell types. We devised the following simple scheme:

1. Each column of C is divided by its mean to ensure that their relative expression values are on the same scale across all cell types; we refer to this column-normalized matrix as C_{col}.
2. Gene expression values smaller than 0.1 times the standard deviation of all nonzero entries of C_{col} are set to be zero. This matrix is used in the gene selection algorithm MRx3 described below.
3. C_{col} is further normalized by dividing each row by its sum; we refer to this matrix as C_{rowcol}. This matrix is used in all gene selection methods except MRx3.

The resulting differential expression scores in C_{rowcol} indicate the fraction of that gene's expression is represented in each cell type, relative to the others; if a given gene has a score of 0.8 for one cell type, for example, the remaining 20% is by construction distributed across all of the other 24 cell types, indicating that this particular gene is strongly informative in uniquely identifying that cell type. One challenge the ideal subset selection must overcome is that heterogeneity in gene expression is unevenly distributed between cell types. For instance, the correlation between gene expression profiles of excitatory neurons in the neocortex from different layers is significantly higher than that between glia and neurons, meaning that care must be taken to ensure that all cell types are adequately represented by the genes chosen.

Gene selection methods:

See **Figure 1b** for a schematic overview of the methods. In each method, the goal is to identify a subset $S \subset G$ of genes from the pool of all genes G that has certain desirable properties. The methods described below differ primarily in how the selection criteria are defined.

1. Minimal Redundancy - Maximum Relevance (mRMR):

The mRMR algorithm attempts to identify the maximally informative set of features with minimal overlap between features, and has been successfully applied to microarray data[18]. In brief, it utilizes a simple greedy search approach to iteratively add genes, one at a time, that maximize an objective function defined by each gene's degree of differential expression across all cell types divided by its similarity to genes that have already been incorporated. Note that this corresponds to the original MRMR algorithm's "quotient" variant[18].

We assume for simplicity that the variance per entry of C_{col} is uniform. Then we define a suitable F-statistic on our data, for any candidate gene $i \in G$ as:

$$F_i = \sum_{j=1}^{N_T} \left(C_{col}(i,j) - \frac{\frac{1}{N_C} \sum_{j=1}^{N_T} C_{col}(i,j))^2}{N_t - 1} \right) \tag{4}$$

This quantity corresponds to the maximum relevance criterion previously proposed[18]. The minimum redundancy criterion[18] is given by the mean of the absolute value of the Pearson correlation between the candidate gene i and the already-selected genes within S:

$$Redund(i|S) = \frac{1}{|S|} \sum_{j \in S} |R(i,j)| \tag{5}$$

Using these two metrics we implemented the following version of the mRMR algorithm that we applied to the rows of C_{col}.

<u>Algorithm MRMR:</u>

1. Initialize $S_0 = \emptyset$
2. For $k \in [1, n_G]$, iterate:

$$g_k = \arg \max_{i \in G - S_{k-1}} \frac{F_i}{Redund(i|S_{k-1})}$$

$$S_k = \{S_{k-1} \cup g_k\}$$

Essentially, this procedure finds, from the currently unselected pool $G - S$, a single candidate gene per iteration that maximizes the F-statistic while minimizing its correlation with those genes that are already in the selected set S. Using the selected genes we finally create row-decimated matrices

$$C_{red} = C(S_{n_G}, :), \qquad E_{red} = E(S_{n_G}, :)$$

2. Minimal Redundancy - Maximum Relevance – Minimum Residual (MRx3):

Although the mRMR approach outlined above produces gene sets that appropriately capture cell type-specific features, it does not consider the impact of these genes on the overall prediction error between E_{red} and $C_{red}D$. The original mRMR algorithm was developed in the context of classification, where the two criteria of relevance and redundancy are appropriate. Here, we have a linear regression problem given by **Equation 1**, hence we have in addition a third criterion: that the reduced matrix produce low residuals. This term should penalize genes for adding exorbitant prediction error, as we anticipated that these genes, while maximally relevant and minimally

redundant with respect to the scRNAseq dataset, would negatively affect the accuracy of the resulting inferred D.

Since our system keeps changing in size during the gene selection process above, we denote $C_k = C(S_k,:)$, $E_k = E(S_k,:)$. The residual vector can be analytically evaluated: $\mathrm{r_k} = \mathrm{E_k} - \mathrm{C_k}(C_k^T C_k)^{-1} C_k^T \mathrm{E_k}$. Suppose we propose to augment the current gene set with a new candidate gene g_i, such that $C_{k+1} = \begin{pmatrix} C_k \\ c_i \end{pmatrix}$; $E_{k+1} = \begin{pmatrix} E_k \\ e_i \end{pmatrix}$, with $c_i = C(g_i,:)$ and $e_i = E(g_i,:)$, the following recursion equation can be demonstrated:

$$\mathrm{r_{k+1}} = \begin{pmatrix} \mathrm{E_k} \\ e_i \end{pmatrix} - \begin{pmatrix} \mathrm{C_k} \\ c_i \end{pmatrix} \left(C_{k+1}^T C_{k+1}\right)^{-1} \left(C_k^T \mathrm{E_k} + g_i^T e_i\right) \tag{6}$$

Now, C_{k+1} has one row more than C_k, hence to evaluate the matrix inverse above, we use the Sherman-Morrison rank-1 update formula[52], and assert that $(C_{k+1}^T C_{k+1})^{-1} \approx (C_k^T C_k)^{-1}$. This approximation is good for $\|C_k c_i\| \ll 1$, which is typically valid since by construction the mRMR criteria ensures that a new candidate gene c_i is near-orthogonal to the current C_k. The approximation is further improved for a sufficiently large selected set, i.e. $|S_k| \gg 1$. In this event, the squared prediction error $\epsilon_k = \left|\left|r_k\right|\right|_F^{\ 2}$ accommodates the following update rule for gene set $S_{k+1} = S_k \cup g_i$:

$$\epsilon_{k+1} \approx \epsilon_k + \epsilon_i \tag{7}$$

$$\epsilon_i = \left\|e_i - C_k (C_k^T C_k)^{-1} C_k^T\ e_i\right\|_2^2 + \|e_i\|_2^2 \cdot \left\|(C_k^T C_k)^{-1} c_i\right\|_2^2 \tag{8}$$

Note, the second term is an upper bound arising from the Cauchy-Schwartz inequality. This update rule is cheap to evaluate since it does not require computing the matrix inverse from scratch, and only involves matrix multiplication. For a given S_k within the MRMR loop described above, ϵ_k is fixed, and ϵ_i can be evaluated for each candidate gene g_i not currently in the selected set; this term is the relative contribution of gene i to the prediction error.

We therefore propose an algorithm, which we call mRMR + Minimum Residual, or MRx3:

<u>Algorithm (MRx3):</u>

a. Run <u>Algorithm mRMR</u> above for $\mathrm{k} \in [1,30]$, i.e. for 30 iterations.

b. For $k \in [31, n_G]$, iterate:

$$g_k = \arg \max_{i \in G - S_{k-1}} \frac{F_i}{Redund(i|S_{k-1}) + \lambda \epsilon_i}$$

$$S_k = \{S_{k-1} \cup g_k\}$$

Here λ is a tunable parameter that controls the weighting of projection error relative to the other two terms. For computational efficiency, we selected 10 genes per iteration of Step b.

3. Entropy:

The rows of C_{rowcol} sum to unity, and we can calculate the entropy, H_i, of gene i as follows:

$$H_i = -\sum_{j=1}^{N_c} C_{rowcol}(i,j)\, log\big(C_{rowcol}(i,j)\big) \tag{9}$$

The genes that are most differential across all cell types are those with minimal entropy. We therefore incorporate all genes with $H_i < h$.

4. Column Approximate Minimum Degree (colAMD):

The colAMD algorithm determines a genes-by-1 row permutation vector $\boldsymbol{p}$ for C_{rowcol} such that the Cholesky decomposition of $C_{rowcol}(\boldsymbol{p},:)^T C_{rowcol}(\boldsymbol{p},:)$ is sparser than that of $C_{rowcol}^T\, C_{rowcol}$. Although the original purpose of colAMD falls outside the scope of our problem, we hypothesized that the reordering itself would separate genes based on their information content, as rows with higher sparsity should be ordered first. We first increase the sparsity of C_{rowcol} by setting all values less than a given informativeness threshold to zero (performance is only mildly sensitive to the choice of threshold), then apply colAMD and take the top n_G entries of $\boldsymbol{p}$ to be our gene set. We used the MATLAB built-in `colamd` to find $\boldsymbol{p}$[53].

5. *Density-based spatial clustering of applications with noise* (DBSCAN):

The DBSCAN algorithm both identifies clusters in noisy data and separates "core" data points from outliers. Since most genes for a given cell type are noninformative, we were interested in applying DBSCAN to each column of C_{rowcol} separately to identify all genes that lie outside of that cell type's main "cluster" of differential expression scores. The algorithm requires a neighborhood search radius, ε, that is inversely related to the number of identified outlier genes; we apply this parameter uniformly across all cell types using the MATLAB built-in function `dbscan`[54].

<u>Estimation of *D* after subset selection:</u>

Each of these methods (genertically denoted by m) depends upon one or two parameters (generically denoted by $\boldsymbol{\theta}$) that controls the number of genes selected. We evaluated subset selection performance across ranges of parameters that result in comparable numbers of included genes, using the reduced matrices C_{red} and E_{red} into **Equation 2** (**Figure 1c**).

Parameter Optimization and Method Validation:

Choosing an appropriate subset selection method and optimizing the number of included genes are critical for ensuring high-fidelity maps across all cell types. In particular, some methods may provide excellent estimates for certain cell types but fail to capture others. We took a holistic approach towards assessing which of the methods above provides the best overall representation of the cell distributions in the mouse brain, relying upon available literature estimates as well as the ordering of neocortical layer-specific glutamatergic cells. We calculated a *sum of fit metrics score*, Σ_{fit}, for each method m across a broad range of values of its associated parameter(s) $\boldsymbol{\theta}$ in the following way:

$$\Sigma_{fit}(m,\theta) = \tau_{adj}(m,\theta) + R_c^{Pv}(m,\theta) + R_c^{Sst}(m,\theta) + R_c^{Vip}(m,\theta) + R_c^{Micro}(m,\theta) \quad (10)$$

where $\tau_{adj}(m,\theta)$ is the adjusted Kendall's rank correlation of the layer ordering for the neocortical layer-specific glutamatergic cells, and $R_c^{Pv}(m,p)$, $R_c^{Sst}(m,p)$, $R_c^{Vip}(m,p)$, and $R_c^{Micro}(m,p)$ are the Lin concordance correlation coefficient values for the cell types Pv, Sst, Vip, and microglia, respectively. We selected the optimal (m,θ) pair based on this heuristic and carried the inferred totals we derived therein throughout the remainder of the study.

Below we describe each of the fit metrics on the right-hand side of **Equation 10** in more detail, as well as the approach we implemented to assess how well our inferred spatial distributions could recreate regional developmental ontology.

<u>Layer ordering:</u>

Seven of the twenty-five cell types represented within our sample are excitatory neurons which have been specifically extracted from individual neocortical layers[6] (**S. Table 1**). Although we could not find corresponding literature estimates at this level of cell type specificity, we expected that we could accurately recreate the appropriate layer ordering of the neocortex from these cell types, because they have mostly nonoverlapping distributions at the spatial resolution of the ISH dataset. Moreover, such an ordering would demonstrate that our inference is accurate not only at the level of anatomical regions, but sub-millimeter voxels as well. We implement the following procedure to infer the neocortical layer ordering per coronal slice:

1. Initialize $y, z = 0$.
2. Map the per-voxel cell counts of each layer-specific glutamatergic neuron across all slices of the brain volume and apply modest smoothing to the resulting images.
3. Determine the center line using MATLAB's `bwskel` of each layer-specific glutamatergic neuron's density "band" within the neocortical voxels of a given slice.
4. Denote the number of cell types that have no neocortical signal by y' and the number that has more subcortical, midbrain, and hindbrain signal than neocortical signal by z'. Let $y = y + y'$ and $z = z + z'$.
5. Calculate the mean distance of each center line to the cortical surface and rank the cell types from closest to farthest.
6. Repeat Steps 2 through 5 for each coronal slice containing neocortical voxels and tabulate the results in a cell-types-by-slices ordering matrix O.

For each column (slice) of O, we produced a corresponding column in the ground-truth ordering matrix O^*, which uses the glutamatergic cell type labels to form the expected layer order among cell types that were present in that slice. Since these orderings contain many identical entries, we utilized a nonparametric rank correlation that accommodates ties, Kendall's τ, between the columns of O and the columns of O^* vertically concatenated. Since we expected these layer-specific neurons to be expressed throughout the neocortex, we incorporated a sensitivity and specificity penalties through y and z, respectively, and calculated the following adjusted correlation:

$$\tau_{adj} = \tau \times \left(1 - \frac{y+z}{7 \times S_{neo}}\right)$$

where s_{neo} is the number of coronal slices containing neocortex.

Direct comparisons to literature:

We utilized existing knowledge about cell counts in the mouse brain where they have been established. Three recent datasets, which we chose for their broad spatial coverage, include quantifications of total cells[3], total neurons[22], and three distinct classes of GABAergic neurons[1], respectively. To assess performance for a specific non-neuronal cell type, we used estimates of microglia density tabulated across multiple studies[19]. For each of these literature estimates, $t^*(J, V_r)$, we provided a corresponding counts prediction based on our inference scheme:

$$t(J, V_R) = \sum_{j \in J} \sum_{k \in V_R} \widehat{D}(j, k)$$

where J and V_R are the sets of cell types and regions represented within the literature value, respectively.

Because we expected to recreate total counts on the same absolute scale as the literature estimates, we required a comparison metric that assesses both the accuracy and precision of our predictions. Although it enjoys widespread use across many applications, the Pearson's correlation (R), which marginalizes out the scale of each vector being compared, is inadequate as a measure of fidelity because it may overestimate the method agreement. We therefore examined the performance of our subsetting and inference using Lin's concordance correlation coefficient (R_c), which performs a pairwise comparison between two vectors relative to the line $y = x$ and is therefore sensitive to differences in absolute scale[55]. By construction, $R_c \leq R$, where equality is achieved only when the best-fit line is $y = x$.

Recreating ontological splits during neural development:

We anticipated that, given the strong relationship regional gene expression shares developmental lineage[2,27], we should be able to recreate developmental ontology using our inferred regional cell type distributions. We therefore performed hierarchical clustering on the regional cell counts matrix, which groups the 212 anatomical regions by their similarity in cell type proportions. We used Ward linkage as the clustering metric, which implicitly requires pairwise Euclidean distance.

To determine how well the levels of the hierarchical clustering tree by region captured developmental staging, we employed a novel algorithm to calculate the adjusted Rand index between our clustering and the ABI developmental atlas, which is based on similarity in gene expression across multiple embryonic and postnatal time points (See **Datasets: Ontology reference** above). The Rand index is defined for two arbitrary clustering methods as the sum of the number of region pairs for which both methods assign them to the same cluster plus the number of region pairs for which they are assigned to different clusters, divided by the total number of region pairs; in other words, it is a measure of pairwise overlap between two clusterings. However, because uneven partitioning of the data into clusters may artificially force more or less overlap between two clusterings, the Rand index is only a useful metric in the context of a null model against which it can be compared. In general terms, the adjusted Rand index (ARI) between two clustering methods X and Y is defined as follows:

$$ARI_{XY} = \frac{RI_{XY} - \langle RI_{null} \rangle}{1 - \langle RI_{null} \rangle} \tag{11}$$

where RI_{XY} is the Rand index between X and Y and $\langle RI_{null} \rangle$ is the expectation value of the Rand index for the null distribution of random clusterings. To generate this distribution, we generated $k = 10000$ random clusterings using the following procedure:

1. Determine the number of regions in each cluster for a given level of the developmental ontology;
2. Using the same number of clusters as the ontology, assign the number of regions per cluster to be a random number between 80% and 120% of the original value;
3. Create a vector of regional cluster labels with the appropriate numbers of regions per cluster and randomly permute it;
4. Repeat Step 2 and Step 3 ($k = 10000$ times).

The resulting random clustering vectors preserve the relative sizes (with some mild stochastic variation) of the clusters in the ground truth against which we are comparing our hierarchical clustering, which allows us to generate an accurate expectation value for calculating the ARI. While the Rand index is strictly bounded between 0 and 1, the ARI can be negative and represents a likelihood that two clusterings overlap more than would be expected by chance, with an ARI of 0 indicating they overlap no better than chance.

For the purposes of this analysis, we separated the forebrain regions (neocortex, hippocampus, olfactory, cortical subplate, hypothalamus, pallidum, striatum, amygdala, and thalamus) from the hindbrain regions (midbrain, cerebellum, pons, medulla). We performed hierarchical clustering on those two subsets of regions individually as described above, then calculated a distribution of ARI values for all levels of division within both ontologies.

REFERENCES

1. Kim, Y. *et al*. Brain-wide Maps Reveal Stereotyped Cell-Type-Based Cortical Architecture and Subcortical Sexual Dimorphism. *Cell* **171**, 456-469 (2017). doi:10.1016/j.cell.2017.09.020
2. Zeisel, A. *et al*. Molecular Architecture of the Mouse Nervous System. *Cell* **174**, 999-1014 (2018). doi:10.1016/j.cell.2018.06.021
3. Murakami, T. C. *et al*. A three-dimensional single-cell-resolution whole-brain atlas using CUBIC-X expansion microscopy and tissue clearing. *Nat. Neurosci*. **21**, 625-637 (2018). doi:10.1038/s41593-018-0109-1
4. Wang, X. *et al*. Three-dimensional intact-tissue sequencing of single-cell transcriptional states. *Science* **361** (2018). doi:10.1126/science.aat5691
5. Erö, C., Gewaltig, M. O., Keller, D. & Markram, H. A cell atlas for the mouse brain. *Front. Neuroinform*. **12** (2018). doi:10.3389/fninf.2018.00084
6. Tasic, B. *et al*. Shared and distinct transcriptomic cell types across neocortical areas. *Nature* **563**, 72-78 (2018). doi:10.1038/s41586-018-0654-5
7. Codeluppi, S. *et al*. Spatial organization of the somatosensory cortex revealed by osmFISH. *Nat. Methods* **15**, 932-935 (2018). doi:10.1038/s41592-018-0175-z
8. Moffitt, J. R. *et al*. Molecular, spatial, and functional single-cell profiling of the hypothalamic preoptic region. *Science* **362** (2018). doi:10.1126/science.aau5324
9. Achim, K. *et al*. High-throughput spatial mapping of single-cell RNA-seq data to tissue of origin. *Nat. Biotechnol*. **33**, 503-509 (2015). doi:10.1038/nbt.3209
10. Satija, R., Farrell, J. A., Gennert, D., Schier, A. F. & Regev, A. Spatial reconstruction of single-cell gene expression data. *Nat. Biotechnol*. **33**, 495-502 (2015). doi:10.1038/nbt.3192
11. Vincent, S. R. & Kimura, H. Histochemical mapping of nitric oxide synthase in the rat brain. *Neuroscience* **46**, 755-784 (1992). doi:10.1016/0306-4522(92)90184-4
12. Björklund, A. & Dunnett, S. B. Dopamine neuron systems in the brain: an update. *Trends in Neurosciences* **30**, 194-202 (2007). doi:10.1016/j.tins.2007.03.006
13. Pazos, A., Cortés, R. & Palacios, J. M. Quantitative autoradiographic mapping of serotonin receptors in the rat brain. II. Serotonin-2 receptors. *Brain Res*. **346**, 231-249 (1985). doi:10.1016/0006-8993(85)90857-1
14. Beier, K. T. *et al*. Circuit Architecture of VTA Dopamine Neurons Revealed by Systematic Input-Output Mapping. *Cell* **162**, 622-634 (2015). doi:10.1016/j.cell.2015.07.015
15. Li, X. *et al*. Generation of a whole-brain atlas for the cholinergic system and mesoscopic projectome analysis of basal forebrain cholinergic neurons. *Proc. Natl. Acad. Sci. U. S. A*. **115**, 415-420 (2017). doi:10.1073/pnas.1703601115
16. Ecker, J. R. *et al*. The BRAIN Initiative Cell Census Consortium: Lessons Learned toward Generating a Comprehensive Brain Cell Atlas. *Neuron* **96**, 542-557 (2017). doi:10.1016/j.neuron.2017.10.007
17. Grange, P. *et al*. Cell-type-based model explaining coexpression patterns of genes in the brain. *Proc. Natl. Acad. Sci. U. S. A*. **111**, 5397-5402 (2014). doi:10.1073/pnas.1312098111
18. Peng, H., Long, F. & Ding, C. Feature selection based on mutual information: Criteria of Max-Dependency, Max-Relevance, and Min-Redundancy. *IEEE Trans. Pattern Anal. Mach. Intell*. **27**, 1226-1238 (2005). doi:10.1109/TPAMI.2005.159
19. Keller, D., Erö, C. & Markram, H. Cell densities in the mouse brain: A systematic review. *Frontiers in Neuroanatomy* **12** (2018). doi:10.3389/fnana.2018.00083
20. Lein, E. S. *et al*. Genome-wide atlas of gene expression in the adult mouse brain. *Nature* **445**, 168-176 (2007). doi:10.1038/nature05453
21. Allen Cell Types Database - Technical White Paper: Transcriptomics. 1–14 (2018) https://portal.brain-map.org/atlases-and-data/rnaseq.
22. Herculano-Houzel, S., Watson, C. & Paxinos, G. Distribution of neurons in functional areas of the mouse cerebral cortex reveals quantitatively different cortical zones. *Front. Neuroanat*. **7** (2013).

doi:10.3389/fnana.2013.00035
23. Sun, Q. *et al*. A whole-brain map of long-range inputs to GABAergic interneurons in the mouse medial prefrontal cortex. *Nat. Neurosci*. **22**, 1357-1370 (2019). doi:10.1038/s41593-019-0429-9
24. Chung, W. S., Allen, N. J. & Eroglu, C. Astrocytes control synapse formation, function, and elimination. *Cold Spring Harb. Perspect. Biol*. **7** (2015). doi:10.1101/cshperspect.a020370
25. Ma, Y. *et al*. A three-dimensional digital atlas database of the adult C57BL/6J mouse brain by magnetic resonance microscopy. *Neuroscience* **135**, 1203-1215 (2005). doi:10.1016/j.neuroscience.2005.07.014
26. Bradl, M. & Lassmann, H. Oligodendrocytes: biology and pathology. *Acta Neuropathol*. **119**, 37-53 (2010). doi:10.1007/s00401-009-0601-5
27. Allen Developing Mouse Brain Atlas - Technical White Paper: Reference Atlases for the Allen Developing Mouse Brain Atlas. 1–10 (2013) http://help.brain-map.org/display/devmouse/Documentation.
28. Gates, A. J. & Ahn, Y. Y. The impact of random models on clustering similarity. *J. Mach. Learn. Res*. **18**, 1-28 (2017).
29. Oh, S. W. *et al*. A mesoscale connectome of the mouse brain. *Nature* **508**, 207-214 (2014). doi:10.1038/nature13186
30. Kosaka, T., Katsumaru, H., Hama, K., Wu, J. Y. & Heizmann, C. W. GABAergic neurons containing the Ca2+-binding protein parvalbumin in the rat hippocampus and dentate gyrus. *Brain Res*. **419**, 119–130 (1987).
31. Hu, J. S., Vogt, D., Sandberg, M. & Rubenstein, J. L. Cortical interneuron development: A tale of time and space. *Dev*. **144**, 3867–3878 (2017).
32. Sherman, S. M. & Guillery, R. W. Functional organization of thalamocortical relays. *J. Neurophysiol*. **76**, 1367–1395 (1996).
33. Harris, K. D. & Shepherd, G. M. G. The neocortical circuit: Themes and variations. *Nat. Neurosci*. **18**, 170–181 (2015).
34. Sun, Y. *et al*. Cell-type-specific circuit connectivity of hippocampal CA1 revealed through cre-dependent rabies tracing. *Cell Rep*. **7**, 269–280 (2014).
35. Meyer, H. S. *et al*. Cell type-specific thalamic innervation in a column of rat vibrissal cortex. *Cerebral Cortex* **20**, 2287-2303 (2010). doi:10.1093/cercor/bhq069
36. Szentágothai, J. The 'module-concept' in cerebral cortex architecture. *Brain Res*. **118**, 244-261 (1975). doi:10.1016/0006-8993(75)90122-5
37. Jones, E. G. & Rakic, P. Radial columns in cortical architecture: It is the composition that counts. *Cerebral Cortex* **20**, 2261-2264 (2010). doi:10.1093/cercor/bhq127
38. Pinto, L. & Dan, Y. Cell-Type-Specific Activity in Prefrontal Cortex during Goal-Directed Behavior. *Neuron* **87**, 437-450 (2015). doi:10.1016/j.neuron.2015.06.021
39. Roseberry, T. K. *et al*. Cell-Type-Specific Control of Brainstem Locomotor Circuits by Basal Ganglia. *Cell* **164**, 526-537 (2016). doi:10.1016/j.cell.2015.12.037
40. Senzai, Y. & Buzsáki, G. Physiological Properties and Behavioral Correlates of Hippocampal Granule Cells and Mossy Cells. *Neuron* **93**, 691-704 (2017). doi:10.1016/j.neuron.2016.12.011
41. Sippy, T., Lapray, D., Crochet, S. & Petersen, C. C. H. Cell-Type-Specific Sensorimotor Processing in Striatal Projection Neurons during Goal-Directed Behavior. *Neuron* **88**, 298-305 (2015). doi:10.1016/j.neuron.2015.08.039
42. Braak, H. & Braak, E. Acta H ' pathologica Neuropathological stageing of Alzheimer-related changes. *Acta Neuropathol* **82**, 239–259 (1991).
43. Braak, H. *et al*. Staging of brain pathology related to sporadic Parkinson's disease. *Neurobiol. Aging* **24**, 197-211 (2003). doi:10.1016/S0197-4580(02)00065-9
44. Mezias, C., LoCastro, E., Xia, C. & Raj, A. Connectivity, not region-intrinsic properties, predicts regional vulnerability to progressive tau pathology in mouse models of disease. *Acta Neuropathol. Commun*. **5** (2017). doi:10.1186/s40478-017-0459-z
45. Fu, H., Hardy, J. & Duff, K. E. Selective vulnerability in neurodegenerative diseases. *Nature*

Neuroscience **21**, 1350-1358 (2018). doi:10.1038/s41593-018-0221-2
46. Fu, H. *et al*. A tau homeostasis signature is linked with the cellular and regional vulnerability of excitatory neurons to tau pathology. *Nat. Neurosci*. **22** 47-56 (2019). doi:10.1038/s41593-018-0298-7
47. Muratore, C. R. *et al*. Cell-type Dependent Alzheimer's Disease Phenotypes: Probing the Biology of Selective Neuronal Vulnerability. *Stem Cell Reports* **9**, 1868-1884 (2017). doi:10.1016/j.stemcr.2017.10.015
48. Skene, N. G. *et al*. Genetic identification of brain cell types underlying schizophrenia. *Nat. Genet*. **50**, 825-833 (2018). doi:10.1038/s41588-018-0129-5
49. Rama Rao, K. V. *et al*. A single primary blast-induced traumatic brain injury in a rodent model causes cell-type dependent increase in nicotinamide adenine dinucleotide phosphate oxidase isoforms in vulnerable brain regions. *J. Neurotrauma* **35**, 2077-2090 (2018). doi:10.1089/neu.2017.5358
50. Arneson, D. *et al*. Single cell molecular alterations reveal target cells and pathways of concussive brain injury. *Nat. Commun*. **9** (2018). doi:10.1038/s41467-018-06222-0
51. Shekhar, K. *et al*. Comprehensive Classification of Retinal Bipolar Neurons by Single-Cell Transcriptomics. *Cell* **166**, 1308-1323 (2016). doi:10.1016/j.cell.2016.07.054
52. Sherman, J. & Morrison, W. J. Adjustment of an Inverse Matrix Corresponding to a Change in One Element of a Given Matrix. *Ann. Math. Stat*. **21**, 124-127 (1950). doi:10.1214/aoms/1177729893
53. Davis, T. A., Gilbert, J. R., Larimore, S. I. & Ng, E. G. A column approximate minimum degree ordering algorithm. *ACM Trans. Math. Softw*. **30**, 353-376 (2004). doi:10.1145/1024074.1024079
54. Ester, M., Kriegel, H.-P., Sander, J. & Xu, X. A Density-Based Algorithm for Discovering Clusters in Large Spatial Databases with Noise. in *Proceedings of the 2nd International Conference on Knowledge Discovery and Data Mining* 226-231 (1996).
55. Lin, L. I.-K. A Concordance Correlation Coefficient to Evaluate Reproducibility. *Biometrics* **45**, 255-268 (1989). doi:10.2307/2532051

CONFLICTS OF INTEREST

The authors have no conflicts of interest to declare.

ACKNOWLEDGEMENTS

The authors would like to acknowledge Dr. Pablo Damasceno for his help with subset selection algorithms and would like to acknowledge Chuying Xia for her prior work in the lab organizing and formatting the raw Allen Institute Mouse Gene Expression Atlas ISH data.

FUNDING

The authors would like to thank the NIH for their generous funding support, which supported this project under Grant Numbers R01NS092802 and R01AG062196.

AUTHOR PERMISSIONS AND APPROVAL

All authors have read the final manuscript and support its submission and potential publication in *Nature Neuroscience*.